Multi-frequency piezoelectric power generator

by

Nassim Ghassoul

Thesis submitted to the university of Oslo in partial fulfillment
of the requirements for the degree of

Master of Science
In
Microelectronics

Universitete i Oslo
September 2007
Oslo

Multi-frequency piezoelectric power generator

Nassim Ghassoul
University of Oslo, 2007
Advisors
Vermesan Ovidiu, Senior Research Scientist
Oddvar Søråsen, Professor

Advances in recent years have seen an increase in the application of wireless sensor networks. Such applications include temperature monitoring, acceleration and pressure sensing in automobiles, medical implants, etc. Low power circuit design has reduced power requirements of these networks considerably. However, batteries are still largely used as power supply. Replacement of these batteries can be problematic in some cases, and methods of scavenging power from ambient sources have been developed in order to make the sensor network self-sustained. Ambient vibrations are a reliable source for energy harvesting in many applications. These vibrations are converted to electrical power through electrostatic or piezoelectric conversion. Piezoelectric conversion is chosen after investigation of the potential power output of each method. This work applies a bending beam concept to the power generator. An estimation of the power output density using a piezoelectric transducer is around a 100 $\mu W/cm^3$ from input vibrations at 120 Hz. The effect of material and design parameters variations are modeled theoretically and through simulations. Design and fabrication of the cantilever structures of the power generator is performed. In addition to the power generator, a biosensor is designed and fabricated. The cantilever structures of both designs are similar and fabricated through the same process. The biosensor employs piezoresistive bridges for the detection of the deflection.

Table of contents

1 **Overview of thesis**

1.1 Concept.......10
1.2 Objectives.......10
1.3 Approach.......11

2 Literature Review

2.1 Energy harvesting for implantable devices.......12
2.1.1 A survey of power sources.......13
2.1.2 Methods available.......14
2.1.3 Conclusions.......15
2.2 Piezoelectric energy generation.......15
2.2.1 Piezoelectricity.......15
2.2.2 Constitutive equations.......22
2.2.3 Coupling factor.......23
2.3 Piezoelectric materials.......24
2.2.1 Issues and considerations.......24
2.3.2 Single crystals.......27
2.3.3 Ceramics.......28
2.4 Piezoelectric generator configuration.......29
2.5 System requirements and constraints.......31
2.5.1 Size constraints.......31
2.5.2 Frequency constraints.......31
2.5.3 Power constraints.......32
2.6 Conclusions.......33

3 Analytical modeling of power generation

3.1 Modeling of a piezoelectric bender....34
3.1.1 Lumped model....34
3.1.2 Bending beam model....37
3.2 Mathematical modeling of the *33* mode cantilever beam....41
3.3 Impedance matching....44
3.4 Power management circuit....46
3.4.1 Power generator as an integrated circuit....46
3.4.2 External power management....47
3.5 Conclusions....48

4 Design and simulations

4.1 Parametric study of beam and *PZT* structure....50
4.1.1 Process description....50
4.1.2 Material properties....52
4.1.2 *FEM* Simulations....53
4.2 Optimization of variables....56
4.2.1 Geometrical beam dimensions....56
4.2.3 Length of interdigitated electrodes....61
4.2.3 Process limitations....62
4.3 Choice of dimensions....63
4.4 Cantilevers for microBUILDER tester....65
4.4.1 Design and specifications....65

5 Processing & Layout

5.1 Process description....67
5.1.1 *MultiMEMS MPW* process....68
5.1.2 Process steps....69
5.1.3 Design specifications/considerations....71

5.2 Design rules....76
5.2.1 Mask set....76
5.2.2 Power generator layout....77
5.2.3 Biosensor layout....79
5.3 Design challenges....80
5.3.1 Process limitations and incompatibilities....81
5.4 Conclusions....81

6 Conclusions

6.1 Discussion....83
6.2 Future work....84

Bibliography 85

Appendix 87

List of symbols

Notation	Description	Unit
b	Width of the electrode	m
C	Capacitance	F
c_{ijkl}	Elastic stiffness constant	N/m^2
d_{ij}	Piezoelectric modulus	m/V
D_i	Electric charge density	C/m^2
ε_{ij}	Dielectric constant	F/m
ε_0	Dielectric constant in vacuum	F/m
E	Electric field	V/m
f	Operating frequency	Hz
F	Force	N
g_{ij}	Voltage constant	Vm/N
i	Current	A
k_s	Stiffness	N/m
L	Length	m
m	Mass	Kg
M	Moment	Nm
P	Power	W
Q	Charge	C
S	Strain	
s_{ijkl}	Elastic compliance	m^2/N
t	Time	s
T_{ij}	Mechanical stress	N/m^2
T_c	Currie temperature	K
U	Energy	J
V	Voltage	V
W	Width	m
σ	Mechanical stress	
ρ	Curvature	m^{-1}

List of figures

Figure 1. Architecture of a wireless sensor node......12

Figure 2. Direct and converse piezoelectric effect......16

Figure 3. Electric dipole moments in Weiss domains......19

Figure 4. Crystalline structure of PZT......19

Figure 5. Movement of charge due to applied stress......20

Figure 6. Orthogonal coordinate system describing properties of a poled ceramic......21

Figure 7. Crystal orientations in a piezoelectric material......21

Figure 8. Movement of the domain walls in a Weiss domain......25

Figure 9. Residual stress in an interdigitated beam......25

Figure 10. Schematic of the *33* and *31* modes......29

Figure 11. Schematic of the interdigitated cantilever beam......30

Figure 12. Energy consumption of a typical wireless sensor......32

Figure 13. Lumped model representation of the piezoelectric bender 34

Figure 14. Basic Cantilever Beam......38

Figure 15. Frequency variations of the beam......40

Figure 16. Frequency variations as a function of the length of the mass......41

Figure 17. Top and side view of an integrated beam......41

Figure 18. Electrical equivalent circuit of a piezoelectric element......44

Figure 19. Electrical circuit equivalent of a piezoelectric bender......45

Figure 20. Architecture of a power harvesting circuit...... 47

Figure 21. Power management and discharge circuits of a power generator......48

Figure 22. Layer description......51

Figure 23. CoventorWare simulations for different lengths of the beam.............................53
Figure 24. CoventorWare simulations for frequency...55
Figure 25. Frequency and stress plots for the variation of mass height...............................55
Figure 26. Schematic setup...56
Figure 27. Beam with suspended mass..57
Figure 28. Frequency response for the varying beam length..58
Figure 29.Frequency response for the varying mass length..58
Figure 30. Frequency response for the varying mass width..59
Figure 31. Frequency response for the varying mass length & mass width..........................60
Figure 32. Frequency response for the varying beam width..60
Figure 33. Beam with interdigitated electrodes...61
Figure 34 IDT electrodes...62
Figure 35. Cantilever with piezoresistive bridge..65
Figure 36. Cross section of the *MultiMEMS* technology showing its main features............68
Figure 37. Layers used in the power generator. 70
Figure 38. Wet etching profile...73
Figure 39. Profile of the transition region...74
Figure 40. Top and side view of the MultiMems die..75
Figure 41. Mask set used in the layout. 76
Figure 42. Layout of the power generator...78
Figure 43. Layout of the biosensor. 80

List of tables

Table 1. A comparison of power sources....13

Table 2. Accelerations and frequencies of ambient vibrations....13

Table 3. Energy storage density comparison....14

Table 4. Coupling coefficients of various piezoelectric materials....23

Table 5. Parameters used in the modeling....39

Table 6. Variables used in the modeling....40

Table 7. Layer thicknesses 52

Table 8. Piezoelectric and ZrO_2 parameters....52

Table 9. Beam dimensions and the resulting frequencies and stress....54

Table 10. Variables used in the simulations....57

Table 11. Dimensions of the cantilevers....64

Table 12. : Resonance frequencies of the cantilevers....64

Table 13. Cantilever dimensions....65

Table 14. *MultiMems* process steps....70

Table 15. Material properties of the silicon substrate....71

Table 16. Material properties of the epitaxial layer....72

Table 17. Membrane thicknesses....72

Table 18. Maximum width of membranes....72

Table 19. Beam dimensions....77

Table 20. Beam dimensions for the biosensor....79

1 Overview of thesis

1.1 Concept

The power generator is based on piezoelectric power conversion. Cantilever beams with a thin film piezoelectric layer convert ambient vibrations to electrical energy. This is possible because of the properties of the piezoelectric material which produces an electric charge when subject to stress. The generated energy is proportional to the amount of stress and a conversion factor which defines efficiency of the conversion. Different materials have different coupling factors, this why the choice of material is an important consideration to maximize the power output. The efficiency of the converter depends however also on the resonance frequency of the system, higher power outputs are achieved when the cantilever vibrates at resonance frequency. This can be controlled through the choice of dimensions and material parameters.

The power management circuits also play an important role in the power generation. Impedance matching can minimize the electrical damping of the material. Power management circuits must induce as few losses as possible.

1.2 Objectives

In this work, design and fabrication of a multi-frequency power generator is performed in a *MEMS* process. Through the design process, relations between the different parameters are determined by modeling and simulations. Processing of the device is considered and performed using a multi project wafer process.

The aim of this work is to design a generator used as a self sustained power supply for a wireless sensor. The generated power output density of around a 100 $\mu W / cm^3$ at a few hundred Hz is expected. A set of different cantilevers are to be used for the generator to operate at several frequencies. Power management is also to be considered.

The design of a biosensor is added to this work in order to fully exploit the possibilities of the process used.

1.3 Approach

Chapter 2

In this chapter, an investigation into power harvesting is performed. Energy sources are compared and ambient vibrations are chosen as energy source. A comparison is then performed between the different energy harvesting methods from vibrations. The piezoelectric energy harvesting is chosen for the power generation.

An introduction to piezoelectricity and its properties is given in order to explain the fundamental principles. Important material parameters are defined, issues and considerations are addressed. The choice of material is then performed. *31-mode* and *33-mode* generation configurations are compared and size, power and frequency constraints are discussed.

Chapter 3

Analytical modeling of the power generator is performed, output power is developed using lumped model equivalents. The bending beam model is addressed and simulations on the frequency is performed. Next, a mathematical modeling develops the relationship between the electrical parameters and the dimensions and material properties. Impedance matching is then considered. Power management circuits are also addressed.

Chapter 4

A parametric study of the power generator is performed in this chapter. The process and material parameters are presented and *FEM* simulations are performed. An optimization of dimensions is done using Saber simulations and a choice of dimensions is made after considering process limitations.

The biosensor is introduced in this chapter, design parameters and specifications are presented.

Chapter 5

Processing and layout of both devices is addressed. The *MultiMems* process flow is described and process parameters are presented. Layout is then performed for the power generator and the biosensor.

Chapter 6

Summaries and conclusions is given as well as a proposal for future work.

2 Literature review

2.1 Energy harvesting for implantable devices

Increased miniaturization of sensors, circuits and wireless communication components has increased the need for reliable wireless power sources. Advances in *MEMS* technology have provided new ways for ambient energy harvesting. Energy can be converted from solar energy, thermal gradients, and vibration-based devices, providing self sustained components. These scavengers may be used to power Body sensor networks [*1*] where fixed energy alternatives are impractical due to the inaccessibility of these sensors, and sensor size is limited by battery size. Power requirement of such network may vary, according to [*2*] an average power consumption of 100 μW is a good estimation. The figure below shows a block diagram of an autonomous micro system with an integrated power source. Power management is done by the *Power module* responsible for recharging the micro battery. Communication between the sensor and the transmitter is done by the power processor.

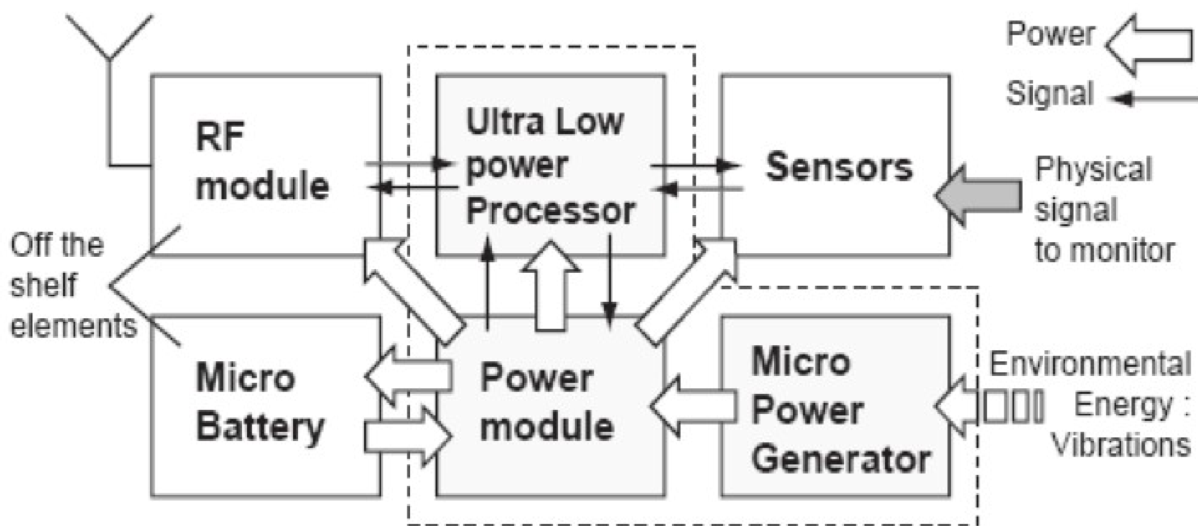

Figure 1 : Architecture of a wireless sensor node.

In this section important aspects of the micro power generator is explored as well as the different methods available for power harvesting, the objective is to determine which method is the most adequate for power generation. Information is mostly based on [*2*].

2.1.1 A survey of power sources

Among power sources available to date the battery is the most widely used, other power sources such as micro heat engines [3], and piezoelectric generators are becoming more and more attractive as power demand decreases. Ambient energy sources can provide enough power to sustain a small device indefinitely.

A comparison between different power sources has been made as shown in table *1*:

	Power density $(\mu W/cm^3)$ **one year lifetime**	**Power density** $(\mu W/cm^3)$ **10 year lifetime**
Solar (outdoors)	15.000- sun, 150-cloudy day	15.000- sun, 150-cloudy day
Solar(indoors)	6-office desk	6-office desk
Vibrations (piezo conversion)	250	250
Vibrations (electro conversion)	50	50
Acoustic noise	0.003 at 75 dB, 0.96 at 100 dB	0.003 at 75 dB, 0.96 at 100 dB
Temperature gradient	15 at 10 c^o gradient	15 at 10 c^o gradient
Shoe insert	330	330
Batteries(non rechargeable lithium)	45	3.5
Batteries(rechargeable lithium)	7	0
Hydrocarbon fuel(micro heat engine)	333	33
Fuel cells (methanol)	280	28

Table 1 : A comparison of power sources.

Taking under consideration the conditions under which the generator will operate, vibration sources seem to offer an interesting and reliable alternative for power generation.

An important consideration is the abundance of vibration sources available for the implanted devices. The human body is always in motion providing a reliable source of vibration through breathing, heart beat and other movements. Table *2* below provides acceleration magnitude and frequency of some fundamental vibration modes for various external sources:

Vibration source	**A** (m/s^2)	**F** (Hz)
Car engine compartment	12	200
Base of 3-axis machine tool	10	70
Blender casing	6.4	121
Cloths dryer	3.5	121
Person nervously tapping their heal	3	1
Car instrument panel	3	13
Door frame after closing	3	125
Small microwave oven	2.5	121
HVAC vents in office building	0.2-1.5	60
Windows next to a busy road	0.7	100
CD on a notebook computer	0.6	75
Second story floor of a busy office	0.2	100

Table 2 : Accelerations and frequencies of ambient vibrations.

2.1.2 Methods available

There are three different methods for energy conversion from vibrations: electromagnetic, electrostatic, and piezoelectric. Researchers have successfully built and tested vibration-based generators using these three types of electromechanical transducers.

For the electro magnetic power generation the current is caused by the relative movement between a coil and a magnetic field. Electromagnetic transducers typically output AC voltages well below *1* volt in magnitude.

Electrostatic generation results from the changes of energy stored in a capacitor as a result of the movement of its conductors. Electrostatic transducers are more easily implemented in standard micro-machining processes. The main disadvantage however, is the necessity of having a separate voltage source to begin the conversion cycle.

Piezoelectric transducers produce voltage as a result of mechanical strain in the piezoelectric material which causes a charge separation across the material. Given appropriate power conditioning and capacitive storage, the resulting power source is sufficient to support networks of low-power wireless nodes. Piezoelectric converters do not require a separate voltage source, but they are not as easily integrated into a micro fabrication process.

The most effective transducer type depends, to a certain extent, on the specific application. A comparison between the effectiveness of the different methods based on the energy storage density was made in table *3*:

Type	**Practical maximum** $(millijoules/cm^3)$	**Aggressive maximum** $(millijoules/cm^3)$
Piezoelectric	35.4	335
Electrostatic	4	44
Electromagnetic	24.8	400

Table 3: Energy storage density comparison.

Practical values represent what is currently achievable with standard materials and processes.

2.1.3 Conclusions

Vibrations is a reliable source for ambient energy harvesting capable of powering small wireless nodes. Based on table *3* piezoelectric converters are capable of converting more power per unit volume than capacitive converters, there is no need for separate voltage source and a voltage output of 3-10 V may be obtained. Piezoelectric thin films can also be integrated into *MEMS* processing. The design of this converter should take into consideration the vibration frequencies to which it is exposed to.

2.2 Piezoelectric energy generation

Advances in Modern electronics has opened up the possibility of powering small wireless computing devices from scavenged ambient power. Piezoelectric power generator has great potential for many applications. Extended device lifetime is advantageous in systems with limited accessibility, such as biomedical implants and self powered micro-devices.

In this section fundamentals of piezoelectricity will be explored as well as the important relations governing the piezoelectric effect. Unless otherwise stated the information is based on [*4,5*] as well as data from some manufacturing companies such as *PI ceramics* [*6*] and *Morgan electroceramics* [*7*]. For additional information and definitions refer to [*8, 9*].

2.2.1 Piezoelectricity

2.2.1.1 Direct and converse piezoelectric effect

The piezoelectric effect describes the direct conversion of mechanical energy electrical to energy or vice versa.

The effect was discovered by the *Curie* brothers in 1880. They demonstrated that some crystals generated electrical polarization from mechanical stress. Pressure was applied to common crystalline materials such as cane sugar, salt and quartz, as a result, electrical charges proportional to the applied stress appeared. Materials having this property are said to be piezoelectric.

The converse effect, mechanical deformation in response to an applied electric field, was demonstrated by *M.G Lippmann* and later confirmed by the *Curie* brothers in 1881.

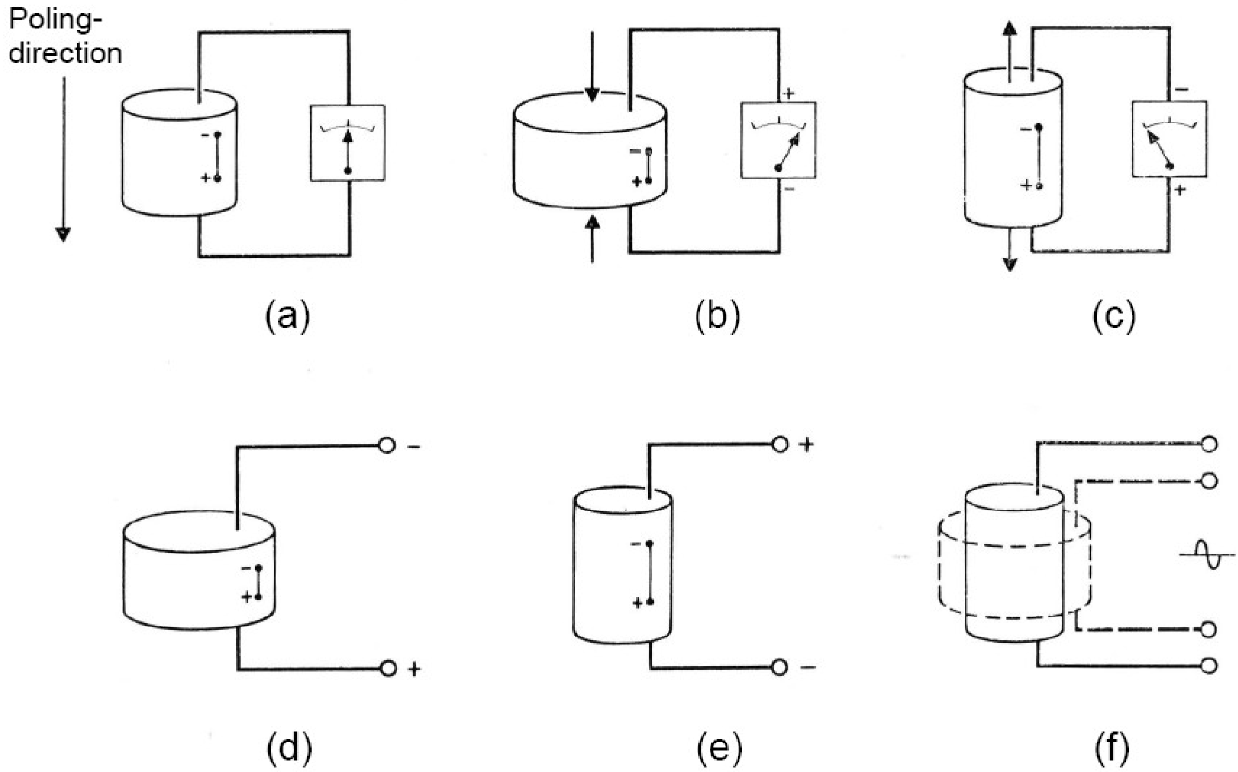

Figure 2 : Direct and converse piezoelectric effect.

Figure 2 shows the direct and converse piezoelectric effect. The poling is shown in figure (a), development of a voltage can be seen in figure (b) as a result of the compression of the material. An opposite voltage results from the stretching of the material, figure (c). The converse effect is shown in figures (d), (e) and (f), the piezoelectric material lengthens and shortens depending on the polarity of the voltage.

The most important relationship for piezoelectric energy harvesting is the linear interaction between the mechanical stress and the electrical charge generated in a crystal, and is expressed through the piezoelectric charge constant d :

$$D_{ij} = d_{ijk} \sigma_{ik} \qquad (2.1)$$

Where D is the charge per area, and σ is the applied stress. The subscripts i and j range from 1 trough 6 and can be replaced by certain rules as we will see later.

2.2.1.2 Material description

Most piezoelectric materials are crystalline solids. These can be either single crystals or polycrystalline like ferroelectric materials. Mono crystals have a continuous crystal lattice throughout the sample, while polycrystals are made of small grains called crystallites, which can be randomly oriented in the material.

The piezoelectric property is due to the absence of a center of symmetry in the crystal lattice. The geometry of the lattice points determines the "system" of the crystal. There are seven crystal systems, each of which is divided into point groups according to their symmetry. Of the 32 point groups, 20 classes can be piezoelectric. A summary of the seven crystal systems and the 32 point groups is given in the appendix.

Physical properties of piezoelectric materials are most conveniently represented as tensors. Depending on the rank of the tensor, each property is described as follows:

- 0th rank tensor (scalar) represents density of a homogeneous solid
- 1st rank tensor (vector) represents polarization: P_i
- 2nd rank tensor represents dielectric susceptibility: χ_{ij}
- 3rd rank tensor represents piezoelectric moduli: d_{ijk}
- 4th rank tensor represents elastic stiffness: c_{ijkl}

An nth rank tensor has 3^n components. Some of these components can be eliminated using the symmetry and point group of the crystal. Most common piezoelectric materials are *4mm* crystal class [*4*], which means a total of 63 components are needed. These constants are reduced to 11 using symmetry rules. Of these constants, 6 represent elastic properties, 3 piezoelectric constants and 2 constant representing permittivity.

2.2.1.3 Ferroelectricity and pyroelectricity

Dielectric materials subject to an electric field *E show* an electric displacement *D* that can be described with the relation:

$$D = \varepsilon_0 \varepsilon_T E \qquad (2.2)$$

Where ε_0 , ε_T represent the relative permittivity of vacuum and the material.

This equation can also be expressed with the polarization *P* of the material due to the applied electric field:

$$D = \varepsilon E + P \qquad (2.3)$$

This polarization is the result of the ionization to a certain degree of the atoms in the material, the cations are attracted to the cathode and the anions to the anode, thus shifting the centers of positive and negative charges in the material. This polarization partially persists in polar materials after removal of the electric field. *Pyroelectric* materials change their polarization upon temperature changes without external electric field. This change depends linearly on the temperature change. If the polar axis of the material changes upon application of an electric field in a different direction, and is maintained upon removal of the electric field, the material is called *ferroelectric*.

Ferroelectric materials have a transition temperature at which the crystal proprieties change. This transition point is called the *Curie* temperature T_C , below this point the material show a strong piezoelectricity, while above they become non polar.

Near the *Curie* temperature the crystalline lattice becomes soft and it becomes possible to pole the material with an electric field. If the ferroelectric material is cooled below Tc without an external field, the ions produce a asymmetry in the crystal. The polarization is not uniform through the crystal and the net polarization is zero, thus the material is not piezoelectric. In order to achieve piezoelectricity, an electric field must be applied above the *Curie* temperature, resulting in a net polarization of the material witch remains after cooling and removal of the electric field. This is illustrated in the figure below:

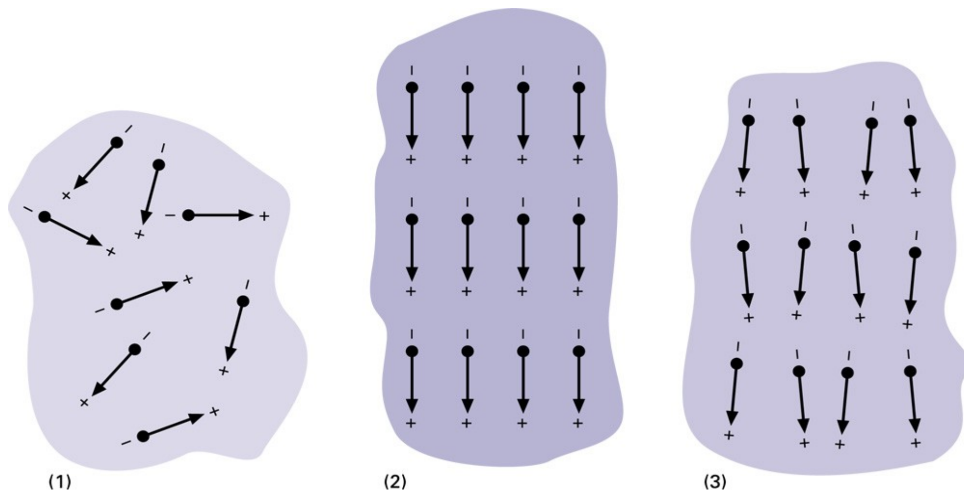

Figure 3 : Electric dipole moments in Weiss domains.

(1) before polarization;
(2) during polarization;
(3) after polarization.

Only ferroelectric materials can be poled, other materials must be used in their single crystal form. Here the orientation of the crystal will become important. It is also important to note that all ferroelectric and pyroelectric materials are piezoelectric.

2.2.1.4 Charge generation

In piezoelectric generators free electrons move by changing the internal electrical field inside the crystal. The charge generation is due to the movement of fixed electrons inside the crystal, as a result of the deformation.

This movement creates a charge dipole, as the positively charged center atoms is no longer in the center of the crystal. As an illustration, a *PZT* crystal is taken as an example.

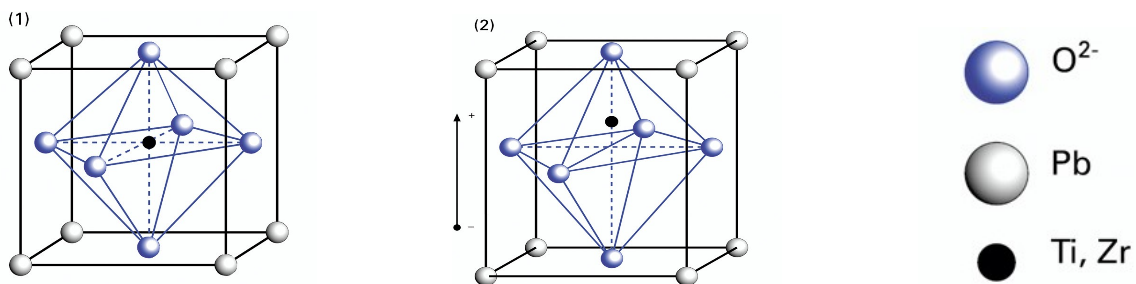

Figure 4: Crystalline structure of *PZT*.

Here the center atom is either Titanium *Ti* or Zirconium *Zr,* surrounded by oxygen and lead atoms. Although *PZT* are not used as single crystals, their polycrystalline structure illustrate

well the formation of the dipole. This dipole creates an electric force in the electrodes, enabling the movement of free electrons as shown below.

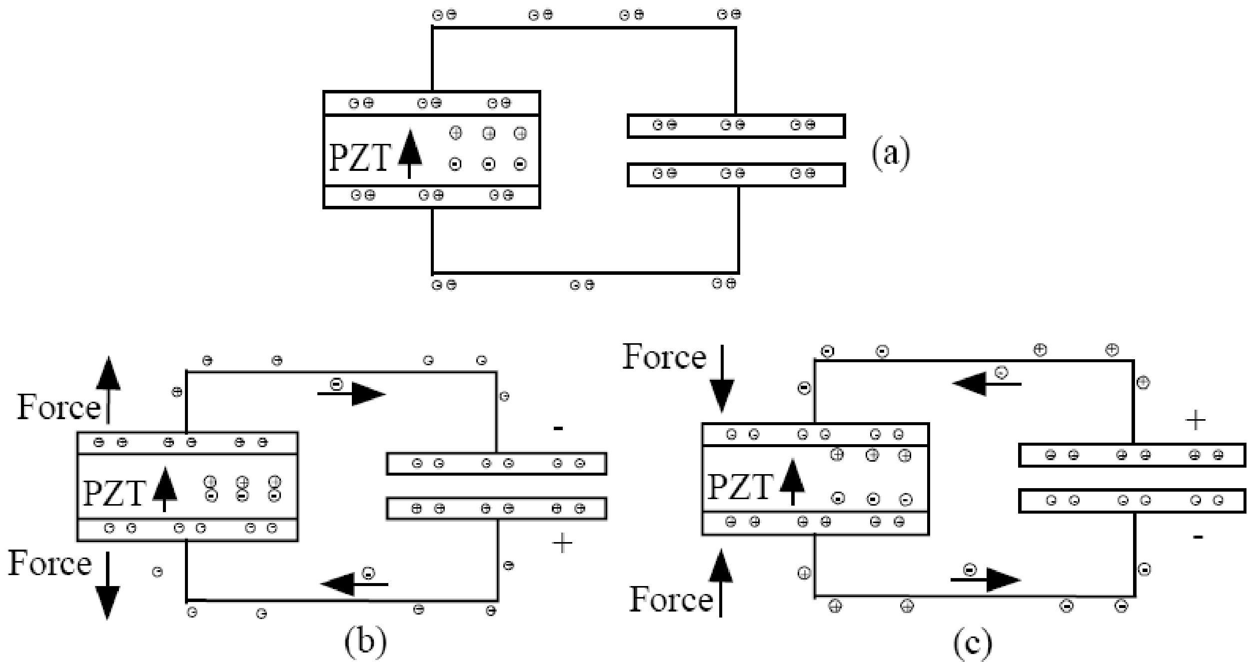

Figure 5: Movement of charge due to applied stress.

(a) with no force; (b) with tensile force; (c) with longitudinal force.

As a result of a tensile force, the internal electric field enables the movement of charge between the electrodes placed on the piezoelectric material. Positive charges are attracted to the upper electrode, negative charges are attracted to the lower electrode, figure (b). In the case of longitudinal force, figure (c), negative charges are attracted to the upper electrode and positive charges are attracted to the lower electrode. In both cases a voltage is generated with opposite polarity.

2.2.1.5 System of notation

Piezoelectricity is an anisotropic effect making it highly dependent on crystal orientation. To account for the different orientations, axes are defined as shown in figure *6*.

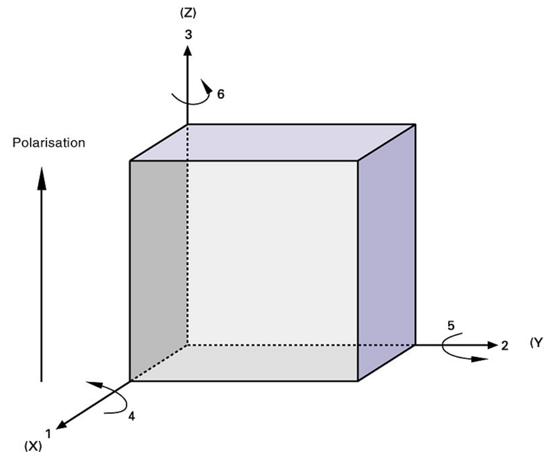

Figure 6 : Orthogonal coordinate system describing properties of a poled ceramic.

Axes *1, 2, 3* coincide with the *X, Y, Z* axes of the crystallography, while 4, 5, 6 are the shear about these axes.

Using these axes the various constants are given two subscripts relating the mechanical and the electrical parameters. The first stands for stimulus while the second represents the reaction of the system. For piezoelectric constants, the first subscript shows the poling direction and the second shows the direction of the applied field or force. In addition super scripts are added to account for boundary or constant conditions. Figure *7* shows crystal orientations in a piezoelectric material.

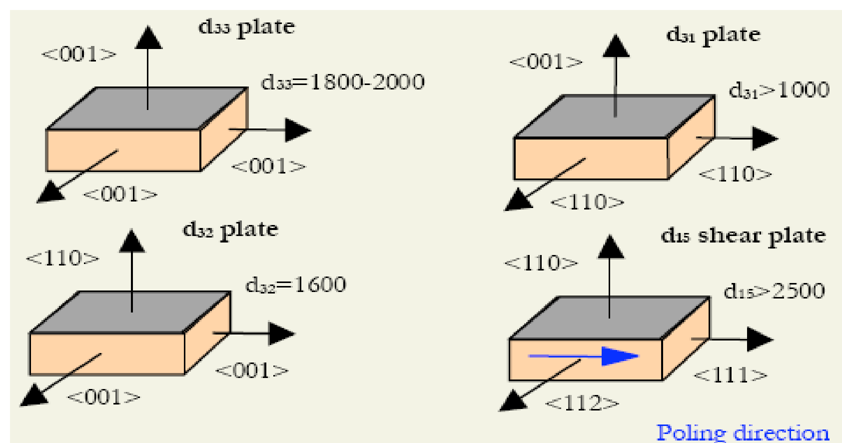

Figure 7: Crystal orientations in a piezoelectric material.

The piezoelectric coupling coefficient seen in equation *2.1* will differ depending on the orientation of the crystal. As seen in the example above *d* is greatest for 15 mode and

smallest for 31 mode. Depending on the material the magnitude relations of these constants is *d15 > d33 > d31.* Although *d15* generates more energy, it is to date very difficult to realize structures using this shear direction. The constant *d33* is about 2,5 times *d31* and generators using this mode have successfully been made using interdigitated electrodes [9]. Still 31 mode is the most widely use to date.

2.2.2 Constitutive equations

Charge generation in a polar material may be induced by an external electric field or by a stress through the piezoelectric effect. Similarly, the mechanical strain in a piezoelectric material may be induced by an electric field through the converse piezoelectric effect or by an external stress through Hooke's law. The coupling of these effects is represented by the constitutive equation:

$$D = d\,T + \varepsilon^{T} E \qquad (2.4)$$

$$S = s^{E} T + d^{t} E \qquad (2.5)$$

Where D is the charge density and S is the strain. The stress T and the electric field E are independent variables in these equations which are only valid under constant electric field and constant stress as indicated by the superscripts.

The coupling coefficient d is a matrix relating the mechanical strain experienced by the material per unit electric field applied, the superscript t represents the transpose matrix. The compliance s is reciprocal to the Young's modulus and is defined as the strain produced per unit of stress. e is the permittivity of the material.

The constitutive equation must also account for the coupling to the different directions within the material of applied stress. Therefore the necessity of a tensor notation.

$$S_{ij} = d_{kij} E_k + s^{E}_{ijkl} T_{kl} \qquad (2.6)$$

$$D_i = \varepsilon^{T}_{ik} E_k + d_{ikl} T_{kl} \qquad (2.7)$$

The indices *i, j, k, l* span 1 through 3, furthermore these indices can be replace by conversion rules replacing the couples *i,j* or *k,l* with simple notations as follows:

$11 \rightarrow 1$, $22 \rightarrow 2$, $33 \rightarrow 3$, 23 or $32 \rightarrow 4$, 31 or $13 \rightarrow 5$, and 12 or $21 \rightarrow 6$

Among the three subscripts converted, the first represents the surface, the other two indices indicate the direction of the electric field, only these are converted to a single subscript.

Using these conversion rules and the symmetry rules of a *4mm* class crystal, the constitutive equations for the short circuit conditions can be written as follows:

$$D_1 = 2 d_{15} T_5 + \varepsilon_{11}^{T} E_1 \quad (2.8)$$

$$D_2 = 2 d_{24} T_4 + \varepsilon_{22}^{T} E_2 \quad (2.9)$$

$$D_3 = d_{31}(T_1 + T_2) + d_{33} T_3 + \varepsilon_{33}^{T} E_3 \quad (2.10)$$

The equations of strain are much more complex and are addressed in appendix. It is also important to note that the constitutive equations will change depending on the symmetry and class of the crystal.

2.2.3 Coupling factor

Another critical factor in piezoelectricity is the coupling factor k relating the amount of stress to the electrical energy converted by the piezoelectric element. This factor accounts for the loss of energy during electromechanical energy conversion.
The coupling coefficient is defined as:

$$k^2 = \frac{E_{mech}}{E_{el}} \quad (2.11)$$

E_{mech} and E_{el} are the mechanical and electrical energies.

This factor is particularly important for the efficiency of the generator as it varies with the choice of material as shown in the table below:

Material	Coupling coefficient (*k*)
Quartz	0.1
AlN	0.24
ZnO	0.33
PZT	0.69

Table 4 : Coupling coefficients of various piezoelectric materials.

The coupling factor of the *PZT* is very high compared to the other piezoelectric materials. This is an important consideration in the choice of piezoelectric material.

2.3 Piezoelectric materials

A wide range of piezoelectric materials have become available thanks to the advanced research into piezoelectric materials, improving material properties and process compatibility has been a major focus. For micro-electromechanical systems piezoelectric materials are divided in two main groups: Single crystals such as quartz, and ceramics such as *PZT*. The choice of material will depend on many properties and process consideration. Issues and constraints involved in the use of a specific material must also be investigated.

2.3.1 Issues and considerations

The most important property of piezoelectric materials for power generation is the value of electromechanical coupling. This determines the effectiveness of the power generator. In addition compatibility with CMOS process and temperature dependence must be taken into account.

Many issues may affect the stability of the material, repeated mechanical and electrical cycling of ferroelectric materials results in a progressive degradation in performance as a function of time. This change in performance depend on the dynamic behavior of the generator, the resonance frequency, mechanical and electrical loads as well as the composition of the material. This section will explore many of the issues responsible for the degradation.

2.3.1.1 Ageing Rates and Time Stability

Most of the properties of piezoelectric ceramics change gradually with time. These changes tend to be logarithmic with time after poling. Ageing is associated with a loss in mobility of the domain walls, they can become trapped in certain positions, which results in a reduction in the ability to generate strain. The ageing rate depends on the ceramic composition and on the manufacturing process and may be influenced by:

- high mechanical stress.
- strong electric depoling field.
- high temperature approaching the T_c

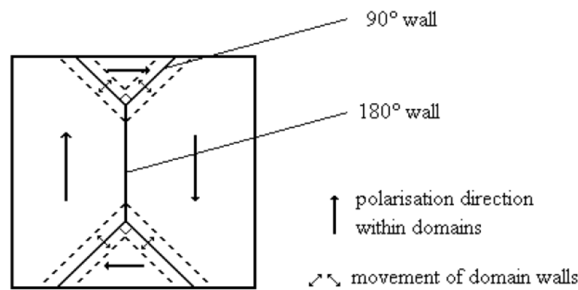

Figure 8: Movement of the domain walls in a Weiss domain.

Structural inhomogeneities such as pores or cracks and charge carriers in the ceramic may also cause ageing.

2.3.1.2 Residual Stress and Piezoelectric Properties

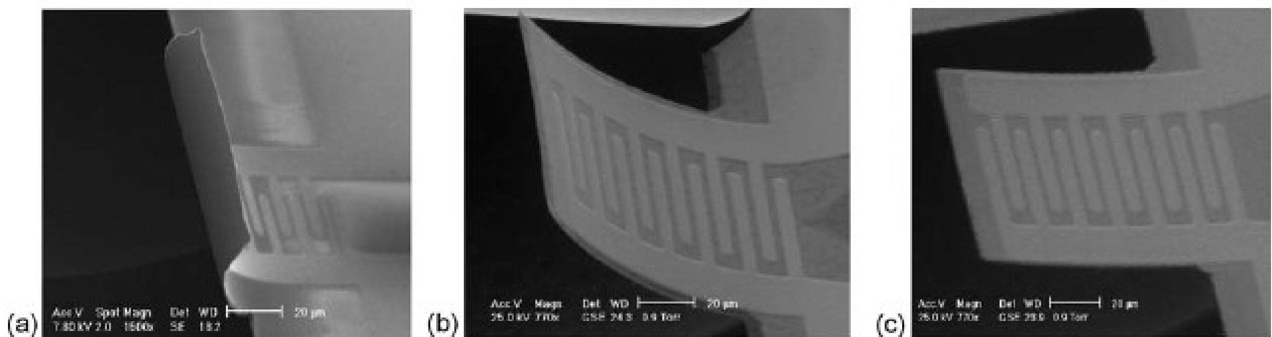

Figure 9 : Residual stress in an interdigitated beam.

Thin films can be subjected to intrinsic stresses during growth at elevated temperatures and extrinsic stresses upon cooling due to differences in the coefficients of thermal expansion (*CTE*). Stresses may also build up on subsequent incorporation into devices. Residual stresses are more pronounced for thinner films, having a more pronounced effect on the piezoelectric properties.

Recent studies have shown that for *PZT* thin films, *d33* measured using interferometric techniques is roughly independent of sample thickness.

2.3.1.3 Piezoelectric Film Quality

The growth of the piezoelectric film can be affected by the substrate onto which it is deposited. The structure of the *PZT* may be changed according to [*12*]. This is a result of the formation of grains during the growth of the film. Surface quality may also affect film quality, the effective elastic property may change as the texture changes. Large anisotropy of the piezoelectric properties has been found in *PZT* films having different textures.
Deposition methods also influence film quality, as *ZnO* is deposited by sputtering, film quality will depend on sputtering conditions

2.3.1.4 Depoling

As mentioned earlier, ferroelectric materials need to be poled to exhibit the piezoelectric effect. Depoling may cause partial or total loss the piezoelectric properties by randomly rearranging the orientation of the domains. The piezoelectric coefficients would decrease as depoling occurs, reaching zero when the alignment of all the domains with respect to the poled direction has been completely lost. Ceramics may be depolarized electrically by exposure to a strong electric field of opposite polarity to the poling field, mechanically when the mechanical stress on a piezoelectric element becomes high enough to disturb the orientation of the domains, or thermally by heating it above the curie point.

2.3.1.5 Micro cracking.

Different strain responses in different regions of the piezoelectric material usually occur as a result of the distortion of the electric field within the material. This can cause regions of high stress in the material resulting in micro cracking. In addition, the changes in strain experienced during domain switching can also lead to the formation of micro cracks. The micro cracks would cause a change in compliance of the piezoelectric material, but degradation in strain performance would make the device unusable before the cracks had grown to a size which could cause structural failure of the device.

2.3.2 Materials available

Among the most widely used piezoelectric materials is Lead Zirconate Titanate *PZT*, Zinc Oxide *ZnO*, Aluminum Nitride *AlN* and polymers such as polyvinylidene fluoride *PVDF.* These materials are used as thin films and are deposition using different techniques. A comparison of the important proprieties and issues will determine the choice of material for the power generator.

2.3.2.1 Single crystals:

Single crystals have a big advantage over polycrystalline materials, they have permanent dipoles and are insensitive to ageing and micro cracking thus making the materials more reliable. They also process higher mechanical quality factors important for resonance applications. Among these materials, *ZnO* has been the most widely researched, mostly because of the ease of fabrication. It is deposited using sputtering and has a good film quality. The coupling coefficient however does not seem to be sufficiently high, nor is it compatible with *CMOS* technology, temperature dependence and low resistivity make it an unlikely candidate or power generation.

AlN however offers some distinct advantages, it has a large resistivity and perform well under temperature variations, it is also compatible with *CMOS* process. The lower coupling coefficient which is crucial in power generation is the major disadvantage.

Despite many attempts mono crystalline *PZT* has not yet been successfully grown, however high performance single crystal ceramics have been realized in the form of new composite materials such as *PMNT*, these materials exhibit exceptionally high strains, they also exhibit very large electromechanical coupling coefficients and offer high dielectric constants and low dielectric losses. These materials are available for use in transducer and actuator devices, but are unfortunately not yet available for *MEMS* devices.

2.3.2.2 Ceramics

By changing the chemical composition of the ceramic, specific properties can be enhanced. Composite materials can be tailored for specific applications making them very attractive for *MEMS* applications.

Because of the ferroelectric nature of *PZT* ceramics, depoling and ageing can occur. Low resistivity and temperature dependence are also issues to consider with common *PZT* materials. However the electromechanical coupling is far superior than its single crystal counterparts making it an excellent material for power generation.

PZT are ceramics based on perovskites [*13*] having a non cubic structure below Tc and a cubic structure above.

According to [*8*] the ceramic materials are arranged in three groups: Hard Materials, Soft Materials and Custom Materials.

Hard Materials

High power or "hard" ceramics can withstand high levels of electrical excitation and mechanical stress. These materials are suited for high voltage or high power generators and transducers. For a more detailed description of the materials refer to [*8*].

Soft Materials

High sensitivity or "soft" ceramics feature high sensitivity and permittivity, but under high drive conditions are susceptible to self-heating beyond their operating temperature range. These materials are used in various sensors, low-power motor-type transducers, receivers, and low power generators. These materials are also described in detail in [*8*].

Custom Materials

Several ceramic materials have been formulated to meet the particular needs of specific applications.

2.4 Piezoelectric generator configuration

The cantilever beam is widely used in sensors and actuators. Beams provide significant deflection and are therefore well suited for power generation applications. *PZT* materials however are not normally used in silicon processing making it particularly difficult to realize the device. Processing possibilities are limited, but the generated power is significantly higher.

A wide variety of other configurations is available [*13*], however only cantilever beams will be considered in this work, this is because of the high strain levels and displacements obtained with beams as well as the ease of processing of such structures.

Bimorph cantilevers are multi layer benders containing a piezoelectric layer bonded to a membrane. Depending on the polarization of the *PZT* material, the cantilever beam can be operated in two modes (*31* and *33*) as shown in the figure bellow:

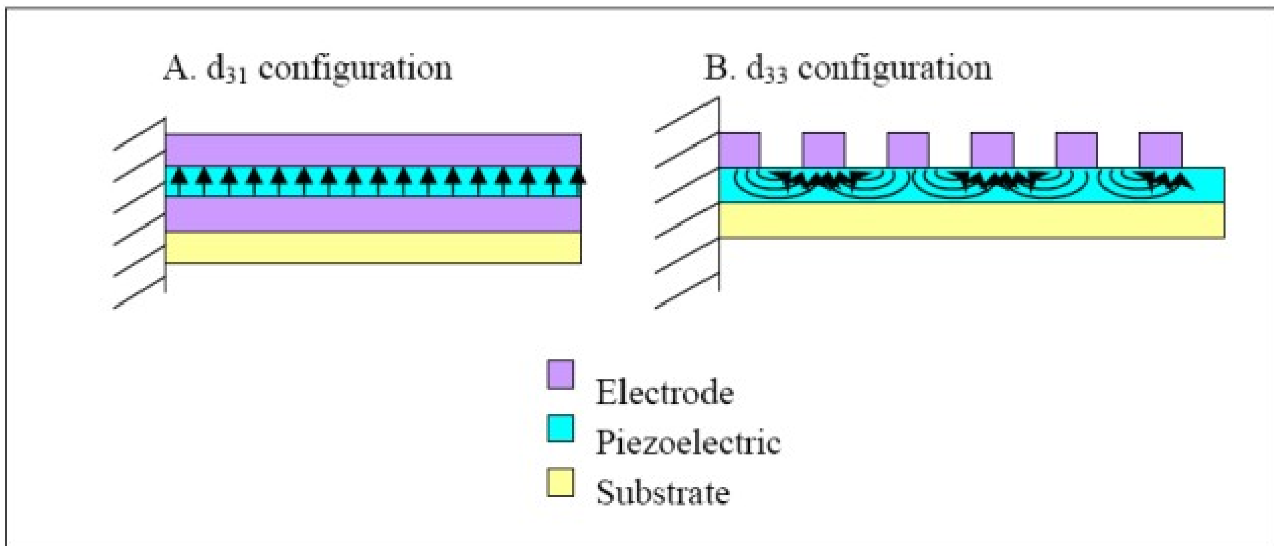

Figure 10 : Schematic of the 33 and 31 modes.

In the *31 mode* configuration the poling direction of the *PZT* is perpendicular to the applied stress, a top and bottom electrode covers the whole upper surface and bottom surface of the *PZT* layer. This configuration requires many mask steps and have a low generated open circuit voltage. The generated voltage from an external stress can be expressed in the equation bellow:

$$V = \sigma_{xx} g_{31} t_{pzt} \qquad (2.12)$$

Where σ_{xx} is the external stress, and g_{31} ($V m N^{-1}$) is the transverse piezoelectric coefficient and t_{pzt} is the thickness of the *PZT* thin film. A power generator using this mode has been constructed at *SINTEF* [*14*].

For the *33* mode configuration the piezoelectric poling direction is in-plane with the applied stress and only an interdigitated top electrode is needed. The generated voltage is higher as expressed in equation (2.12) , and the required mask steps are fewer.

$$V = \sigma_{xx} g_{33} L \qquad (2.13)$$

Where L is the distance between the interdigitated (*IDT*) electrodes. The use of this interdigitated configuration allows for higher generated voltages as g_{33} is considered to be twice as high as g_{31} , L is also much greater than t_{pzt} yielding a much higher generated voltage [*14*].

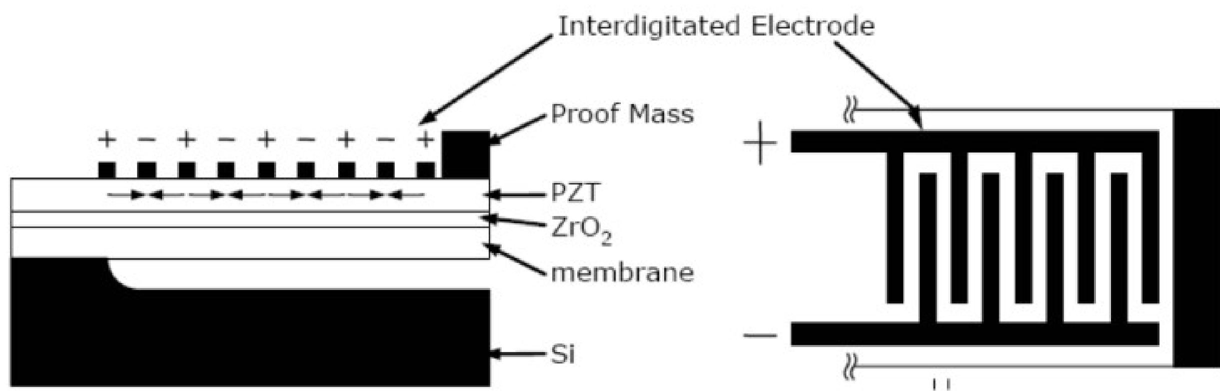

Figure 11 : Schematic of the interdigitated cantilever beam.

A schematic of the cantilever beam and its interdigitated electrodes are shown in the figure above. The beam is made of a membrane layer in silicon supporting a buffer layer of Zirconia and the *PZT* layer. *ZrO2* has previously been used as buffer layer for other power generators [*15*]. The electrode are composed of gold.

As for the dimensions process parameters have to be taken into consideration, currently available process has a minimum thickness of $3.2\mu m$ for the membrane. The piezoelectric effect is not influenced by the thickness of the *PZT* layer [*16*] so the thickness is set to $0.5\mu m$ for the *PZT*. To obtain the desired resonant frequencies, length and width of the beam are modulated.

2.5 System requirements and constraints

In order to design an efficient power generator a set of requirements must be met. As an implantable device, size constraints are imposed as well as the operating frequency under which it will function. Wireless sensor nodes connected to the power generator also have their power management constraints.

2.5.1 Size constraints

Standard wireless technologies such as *Bluetooth* [*17*] and *ZigBee* [*18*] offer low-cost, low-power self managed wireless sensor networks. *BlueTooth* is a well established technology with power requirements around $40-60\,mW$. *ZigBee* however, is an emerging wireless standard for low data rate, low-power applications, with potential applications in wireless medical sensors. Platforms still in the research stage approach an overall power consumption in the hundreds of micro watts [*2*].

A vibration based piezoelectric generator would produce enough power for such a wireless node replacing battery driven sensors. The target size of the generator is based on the typical size of a wireless sensor node [*18*]. As the power is directly related to size as in batteries an overall size of $1\,cm^3$ for the device is chosen, giving a size of approximately $0.5\,cm^3$ for the power generator.

Manufacturing considerations must also be taken into account, the final size of the device will depend on its configuration and whether the power management circuit is integrated on the same chip or not. This will be investigated later in this work.

2.5.2 Frequency constraints.

In order to maximize the power output, the device must be designed to resonate at the fundamental vibration frequency, as a multi frequency generator a range of frequencies must be chosen containing the different resonant frequencies for the beams. As seen in table *2* the natural frequencies surrounding the human body are in the range $1-200\,Hz$, however these frequencies are difficult to obtain within $0.5\,cm^3$. A frequency range of $50-250\,Hz$ is chosen

as a starting point for the generator. Final frequencies will be determined by the manufacturing possibilities.

An other reason why low frequencies are chosen is that the power output is proportional to A^2/ω where ω is the frequency of the fundamental vibration mode and A is acceleration, this will be addressed furthermore in the modeling chapter.

2.5.3 Power constraints.

As seen in previous sections a power output in the order of a few hundred μW is needed to power a wireless sensor node. This power is managed according to the operation of the sensor. Figure *12* gives a simple power consumption diagram for a typical sensor.

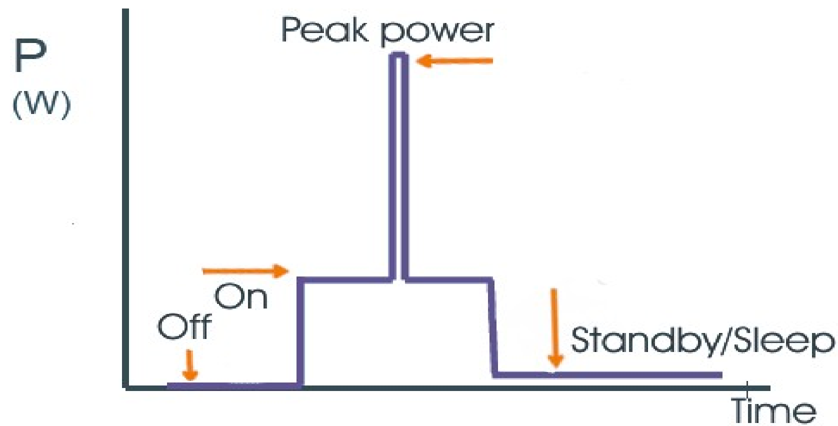

Figure 12: Energy consumption of a typical wireless sensor.

The *On* state may refer to data acquisition or other tasks, the *peak power* is reached during data transmission to other devices, the rest of the time the sensor is set to standby where little energy is consumed. This operation makes it possible to realize low power systems where the energy harvesting can be used as power supply. The aim of this work is to obtain power levels of around a few hundred μW .

2.6 Conclusion

So far in this work most of the aspects of the power generator have been determined. Piezoelectric energy harvesting was found to be the most efficient way to harvest low level vibrations, *PZT* ceramics was chosen as the piezoelectric material and a general understanding of the power generation mechanism was introducer. The interdigitated *33-mode* of the beam was chosen due to the high power output generated with this configuration, as well as the operating frequencies and power output expected from this device. The size of the generator is to be limited to approximately $0.5\,cm^3$ depending on processing possibilities. The number of beams will also depend on processing.

3 Analytical modeling of power generation

Through the literature review, the choice of energy generating method has been made as well as the most suited configuration. In this chapter the design of the system is performed, dimensions and operating parameters are determined through modeling and simulations. Processing is considered and power management is investigated. The modeling is based on general beam theory [*21*] and other related work with piezoelectric power generation [*19*].

3.1 Modeling of the piezoelectric bender

3.1.1 Lumped modeling

An estimation of the power generated from a piezoelectric element can be performed using the spring, mass and damper system. Mechanical properties of a real piezoelectric element can be determined using this simple model. The spring, mass, and damper system is shown in Figure 13.

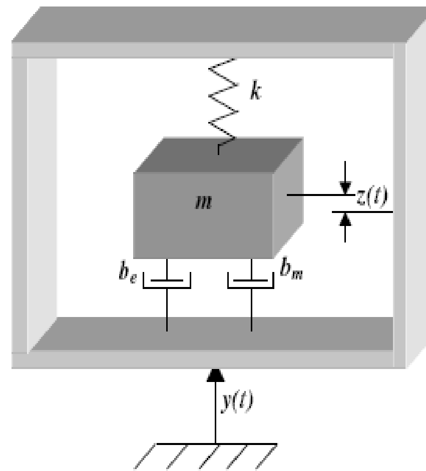

Figure 13 : Lumped model representation of the piezoelectric bender

The system is composed of a rigid box subject to vibrations $y(t)$ and a mass m suspended by a spring *k*. b_e and b_m are electrical and mechanical damping. The relative movement of the mass is represented by $z(t)$.

In this model, some of the energy is lost through the mechanical damping, the rest is

converted to electrical energy. The spring represents here the ideal compliance, the mass is an energy storage element, and the damper accounts for internal mechanical losses.
When subject to a sinusoidal excitation $y(t)$:

$$y(t)=Y\sin(\omega t) \tag{3.1}$$

The mechanical equation of motion is given by :

$$m\ddot{z}+(b_e+b_m)\dot{z}+kz=-m\ddot{y} \tag{3.2}$$

Where

z mass displacement;

$\dot{z}$ mass velocity;

$\ddot{z}$ mass acceleration;

m the effective mass;

b_e electrical damping;

b_m mechanical damping;

k stiffness;

The displacement can be given as:

$$z(t)=\frac{-(Ym\omega\cos(\omega t+\phi))}{\sqrt{(((b_e+b_m)\omega)^2+(m\omega^2-k)^2)}} \tag{3.3}$$

the electric force generated is given by:

$$f_e(t)=b_e\dot{z}(t)=\frac{(Yb_em\omega^3)}{\sqrt{(((b_e+b_m)\omega)^2+(m\omega^2-k)^2)}}\sin(\omega t+\phi) \tag{3.4}$$

power can then be determined as :

$$p(t)=f_e(t)\dot{z}(t)=\frac{(Y^2b_em^2\omega^6)}{(((b_e+b_m)\omega)^2+(m\omega^2-k)^2)}\sin^2(\omega t+\phi) \tag{3.5}$$

the average power is given by:

$$P=\frac{1}{T}\int p(t)dt=\frac{1}{2}\frac{(Y^2b_em^2\omega^6)}{[(((b_e+b_m)\omega)^2+(m\omega^2-k)^2)]} \tag{3.6}$$

Using : $\omega_n=\sqrt{(\frac{k}{m})}$, $b_e=2m\xi_e\omega_n$ and $b_m=2m\xi_m\omega_n$

ξ_e and ξ_m are the electrical and mechanical damping ratios.

the normalized power is as follows:

$$P=\frac{(Y^2\xi_e m\omega_n^3(\frac{\omega}{\omega_n})^6)}{[((2(\xi_e+\xi_m)(\frac{\omega}{\omega_n}))^2+(1-(\frac{\omega}{\omega_n})^2)^2)]} \quad (3.7)$$

using the acceleration A

$$Y=\frac{A}{\omega^2} \quad \Rightarrow \quad P=\frac{(\frac{(A^2\xi_e m)}{\omega_n}(\frac{\omega}{\omega_n})^2)}{[((2(\xi_e+\xi_m)(\frac{\omega}{\omega_n}))^2+(1-(\frac{\omega}{\omega_n})^2)^2)]} \quad (3.8)$$

At the resonance frequency, the power is written as:

$$P=\frac{(mA^2\xi_e)}{[4(\xi_e+\xi_m)^2\omega_n]} \quad (3.9)$$

The generated power is proportional to the moving mass and the square of the acceleration. To maximize the power, the stiffness of the spring must be chosen so that the resonance frequency coincides with the frequency of the excitation and the electrical damping is equal to the mechanical damping.
It should also be noted that as the displacement decreases with the increase of frequency. The power decreases as well, because the decreasing input vibration amplitude dominates the increasing frequency contribution.

In order to maximize electrical power output, the system must be designed to vibrate at the resonance frequency. According to [*10*] generated power decreases by half if the frequency deviation is 2% from the resonant frequency. More than 5% deviation and the generated power is completely diminished.

The power can also be optimized using the electrical damping ratio. ξ_e is a function of circuit parameters and can be designed to be as small as possible. Output power is also

optimized for low ξ_m and equal to ξ_e .

The larges possible mass should be used in the generator since the output power is directly related to the suspended mass.

3.1.2 Bending beam model

The elastic modulus of piezoelectric materials is an important parameter in determining the resonant frequency of the beam, a change in this modulus will result in a change in the frequency of the device.

There are three basic possibilities for circuit conditions applied to a piezoelectric element of a resonator. The total capacitance is equal to the sum of the contributions from the piezoelectric layer and the shunt capacitance.

When the piezoelectric is left open circuited; the capacitance is equal to that of the piezoelectric layer. In this situation, the effective modulus E_p of the piezoelectric layer is a function of both this capacitance, and the material compliance of the layer, given by:

$$E_{oc}=E_p=\left(s^E-\frac{d^2}{\epsilon_p}\right)^{-1} \tag{3.10}$$

This is the maximum stiffness condition of the beam. ϵ_p is the relative permittivity of the piezoelectric material and d is the piezoelectric modulus.

If the electrodes are short circuited, the capacitance of the piezoelectric element is equal to zero and the electromechanical coupling does not affect the stiffness. Consequently, the Young's Modulus of the piezoelectric layer is simply equal to the inverse of the compliance for the piezoelectric material:

$$E_{sc}=E_p=(s^E)^{-1} \tag{3.11}$$

This results in the minimum stiffness condition for the piezoelectric layer, which is analogous to the lower frequency limit of resonators.

Since these two conditions define the upper and lower limits on the variable stiffness of the system, they are also the stiffness terms used to calculate the limits on the range of frequencies. A capacitance can also be added in parallel with the piezoelectric layer to vary the stiffness between its two extreme conditions, in which case the modulus is equal to:

$$E_p = (s^E + \frac{d^2}{\epsilon_p} + Z_{sh})^{-1} \tag{3.12}$$

where Z_{sh} is the impedance of the shunt capacitor. Consequently, the frequency can be adjusted to any value between its upper and lower limits by selecting the appropriate capacitive shunt.

According to simple beam theory, the frequency can be represented as in equation (3.13) . The model is simplified and is shown in figure *14*.

$$\omega = \sqrt{(\frac{K_{eff}}{m_{eff}})}\ ; \tag{3.13}$$

Where:

$$K_{eff} = \frac{(3\,E\,I_{eff})}{L^3} \tag{3.14}$$

Where K_{eff} is the effective stiffness of the beam and I_{eff} is the effective moment of inertia. This moment is to be calculated. It is possible from there to simulate the frequency variations with the variation of the beam dimensions.

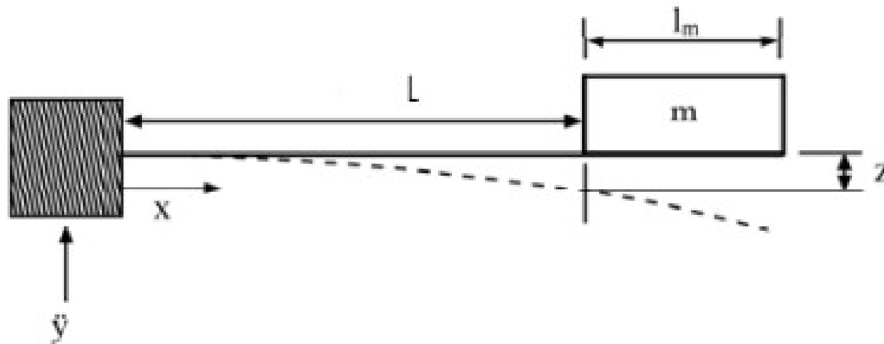

Figure 14: Basic Cantilever Beam.

The relationship between the different parameters can be demonstrated through the

following relationship which is based on the simple beam theory:

$$f(1)=\frac{1}{(2\pi)}\sqrt{\left(\frac{(3WEt^3)}{(12L^3(m+0.236m_b))}\right)} \tag{3.15}$$

Where m_b is the mass of the beam, m is a suspended mass, E is the elastic modulus. W and L are the width and length of the beam.

Equation (3.15) gives the resonant frequency for the first fundamental mode. Variations of the length of the beam or the size of the suspended mass would inversely affect the resonant frequency. However, this is a simplified model and is not accurate enough to determine the physical dimensions of the beam. CoventorWare simulations must be conducted using a *FEM* method. Equation (3.15) gives however an indication of the length and dimensions of the mass making it easier to determine the range of the different parameters.

Simulations have been performed in Matlab and CoventorWare to determine the length and width of the beam resulting in the lowest resonant frequency.

Tables *5* and *6* represent the constants and variables used in the modeling of the system.

Constants	**Unit**	**Description**
$t=3.35*10^{-6}$;	(m)	Thickness of the beam.
$\rho_b=2330$;	(Kg/m^3)	Density of beam.
$h_e=1.2*10^{-6}$;	(m)	Thickness of electrode.
$\rho_e=19300$;	(Kg/m^3)	Density of electrode.
$W_e=3*10^{-6}$;	(m)	Width of electrode finger.
$b=6*10^{-6}$;	(m)	Spacing between fingers.
$E=166*10^{6}$;	(Pa)	Young's module.
$\rho_m=2200$;	(Kg/m^3)	Density of mass.
$h_m=23*10^{-6}$	(m)	Height of mass.

Table 5 : Parameters used in the modeling.

Variables	Unit	Description
$L_m=300*10^{-6};$	(m)	Length of mass.
$W:$	(m)	Width of beam.
$L:$	(m)	Length of beam.
$n=57;$		number of fingers.
$L_e=W;$	(m)	Length of fingers.
$l_e;$	(m)	Length of electrode.
m	kg	Mass.
m_b	kg	Mass of beam.

Table 6: Variables used in the modeling.

Using equation (3.15) and plotting the frequency variation as a function of the variation of the length gives the following figure:

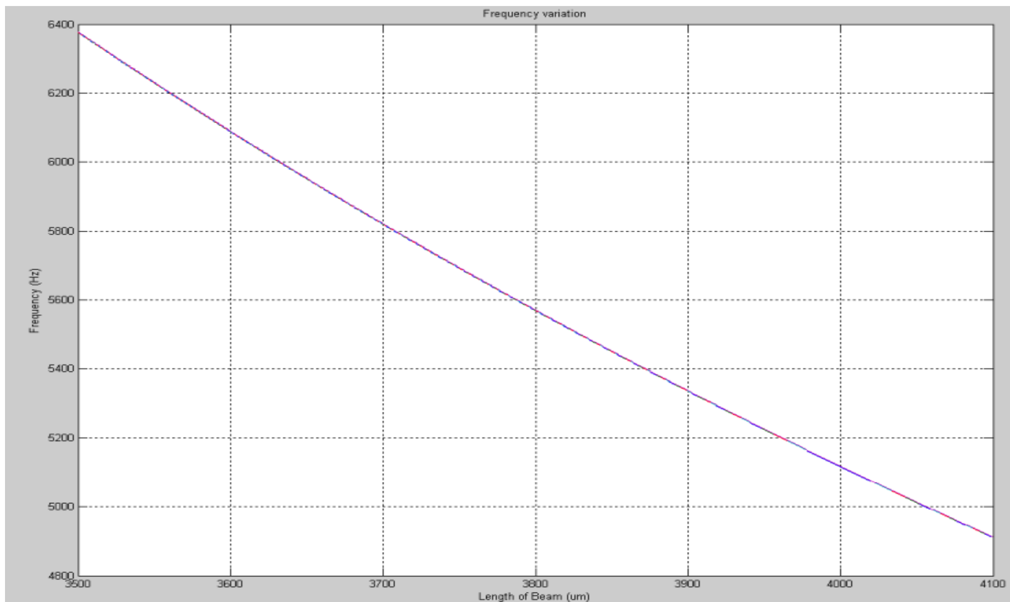

Figure 15 : frequency variations of the beam.

Frequency decreases with the increase of the length of the beam, for the optimal length chosen simulations are performed in CoventorWare giving the longest possible beam. *FEM* simulations are addressed later.

For the second set of simulations, the length of the mass has been varied from $300-500\,\mu m$. The number of electrodes is increased from 25 to 150. In this model, this will only affect the mass of the beam which will increase, a more detailed model is needed to account for the effect of the electrodes on the frequency, this will be addressed later. The length of the beam is set to $4{,}1\,mm$ and the width to $250\,\mu m$.

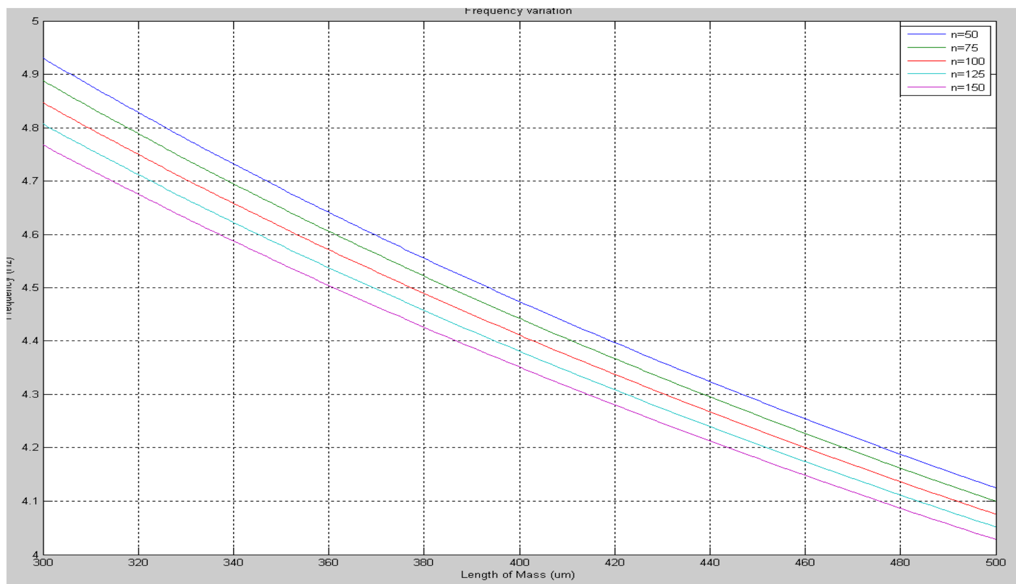

Figure 16 : frequency variations as a function of the length of the mass.

The increase of the length and the number of electrodes also affect the resonant frequency.

3.2 Mathematical modeling of the *33* mode cantilever beam

The electrical parameters can be extracted using the constitutive equations for the piezoelectric layer, the free capacitance and the generated voltage can be found. In this section, the electric constitutive equations are developed using parameters from a *6mm* class piezoelectric crystal *PZT5H.*

This modeling is performed to determine the relationship between the generated voltage and the dimensions of the beam.

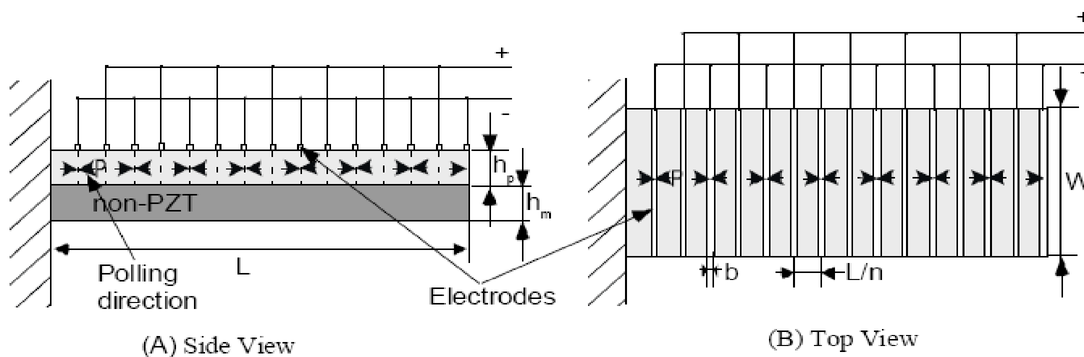

Figure 17 : Top and side view of an integrated beam.

The figure above represents the part of the beam covered by the piezoelectric material. In this figure the width of the electrodes is the same as the width of the beam.

The constitutive equations of an interdigitated cantilever beam can be written as:

$$S_1 = s_{33}^E \rho_1 - d_{33} E_3 \qquad (3.16)$$

$$D_3 = -d_{33} \sigma_1 - \epsilon_{33}^T E_3 \qquad (3.17)$$

Where and

D is the charge density; s is the elastic compliance;

S is the strain; σ is the mechanical stress;

E is the electric field; ϵ_{33}^T is the dielectric constant;

The poling of the piezoelectric layer is changed in the interdigitated case.

The general energy for piezoelectric materials is given by :

$$U = \frac{1}{2} S * T + \frac{1}{2} Q * E \qquad (3.18)$$

Were T is the stress and Q is the charge. From this the energy generated from the piezoelectric structure can be written as:

$$d\,U_p = \frac{1}{2}(s_{33}^E \sigma_1 - d_{33} E_3)\sigma_1 + \frac{1}{2}(-d_{33}\sigma_1 + \epsilon_{33}^T E_3) E_3 \qquad (3.19)$$

$$d\,U_p = \frac{1}{2} s_{33}^E \sigma_1^2 - d_{33} E_3 \sigma_1 + \frac{1}{2} \epsilon_{33}^T E_3^2 \qquad (3.20)$$

The neutral surface is the surface in the cantilever where no stress is generated by external forces. This neutral surface is not in the center of the beam in the interdigitated case. The neutral surface for the interdigitated beam can be written as :

$$z_{c3} = \frac{1}{2} \frac{(h_p^2 s_m - h_m^2 s_{33}^E)}{(h_m s_{33}^E + h_p s_m)} \qquad (3.21)$$

where h_m and h_p are the thickness of the substrate layer and the piezoelectric layer. s_m is the compliance of the substrate.

The stress is then calculated from the equation of moment:

$$M = \int \sigma(\rho(x, M, E_3), E_3) z\, dz \qquad (3.22)$$

The moment is represented as a function of the curvature $\rho(x, M, E_3)$ and the electric filed.

Using the equation of curvature and solving in terms of force and electric field:

$$\rho = \frac{-((12 s_m s_{33}^E (s_{33}^E h_m + s_m h_p)(L-x)))}{(B_{33} W)} F_0 + \frac{(6 \mathrm{d}_{33} s_{33}^E s_m h_p h_m (h_m + h_p))}{B_{33}} E_3 \quad (3.23)$$

where $B_{33} = s_m^2 h_p^4 + 4 s_{33}^E s_m h_p^3 h_m + 6 s_m s_{33}^E h_p^2 h_m + 4 s_{33}^E s_m h_p h_m^3 + (s_{33}^E)^2 h_m^4$. Using the stress equation as a function of the curvature:

$$\sigma_1 = \frac{1}{(s_{33}^E)}(-\rho(z - z_{c3}) + d_{33} E_3) \quad (3.24)$$

substituting in the expression of the energy results in

$$d U_p = \frac{1}{2} s_{33}^E [\frac{(-\rho(z - z_{c3}) + d_{33} E_3)}{(s_{33}^E)}]^2 - d_{33} [\frac{1}{(s_{33}^E)}(-\rho(z - z_{c3}) + d_{33} E_3)] E_3 + \frac{1}{2} \epsilon_{33}^T E_3^2 \quad (3.25)$$

setting the number of electrodes to *n+1* with a width *b*. The total energy is given by summation of each segment between the electrodes and integrating over the entire beam.

Using the following substitutions:

$E_3 = \frac{V}{h} = \frac{V}{(L/n)}$ and $k_{33}^2 = \frac{d_{33}^2}{(\epsilon_{33}^T s_{33}^E)}$, and $S_{h3} = s_{33}^E h_m + s_m h_p$;

the resulting charge can be determined:

$$Q = \frac{-(3 n d_{33} s_{ee}^E s_m h_m h_p (h_m + h_p)(L - n b))}{B_{33}} F_0 \quad (3.26)$$

$$+ \ (\frac{(n^2 \epsilon_{33}^T h_p W (L - n B))}{L^2})[1 + [\frac{(3 s_{33}^E s_m h_m^2 h_p (h_m + h_p)^2)}{(S_{h3} B_{33})} - 1] k_{33}^2] V$$

Generated charge from force is :

$$Q_{gen} = \frac{(3 n d_{33} s_{33}^E s_m h_p h_m (h_p + h_m)(L - n * b))}{B_{33}} F_0 \quad (3.27)$$

and total open circuit capacitance is

$$C_{free} = \frac{(n^2 \epsilon_{33}^T h_p W (L - n b))}{L^2} (1 + k_{33}^2 ((\frac{(3 s_{33}^E s_m h_m^2 h_p (h_m + h_p)^2)}{(S_{h3} B_{33})}) - 1)) \quad (3.28)$$

Generated voltage open circuit :

$$V_{gen}=\frac{Q_{gen}}{C_{free}}=\frac{(3\,d_{33}s_{33}^{E}s_{m}h_{m}(h_{m}+h_{p})\,L^{2})}{(n\,\epsilon_{33}^{T}\,W\,B_{33}^{2}(1+(\frac{(3\,(s_{33}^{E})^{2}\,s_{m}h_{p}h_{m}^{2}(h_{m}+h_{p})^{2})}{(S_{h3}\,B_{33})}-1)\,k_{33}^{2}))}F_{0} \quad (3.29)$$

and the total electrical energy generated is

$$U_{gen}=Q_{gen}V_{gen}=\frac{(9\,d_{33}^{2}(s_{33}^{E})^{2}\,s_{m}^{2}h_{m}^{2}(h_{m}+h_{p})^{2}(L-n\,b)\,L^{2})}{(\epsilon_{33}^{T}\,W\,B_{33}^{2}(1+(\frac{(3(s_{33}^{E})^{2}s_{m}h_{p}h_{m}^{2}(h_{m}+h_{p})^{2})}{(S_{h3}B_{33})}-1)\,k_{33}^{2}))}F_{0}^{2} \quad (3.30)$$

From the equation of voltage, it is clear that the power is maximized for longer beams with small widths. A small number of fingers and high piezoelectric constant are favorable.

This modeling does not account for the closed circuit operation of the power generator. This is addressed in the next section.

3.3 Impedance matching

The piezoelectric material can also be modeled using an electric circuit equivalent. The piezoelectric material have internal impedances which dissipate energy, these impedances are responsible for the loss of some of the generated power. Equivalent electrical circuits can be used to model these effects.

The equivalent model of the piezoelectric element is shown in figure *18*.

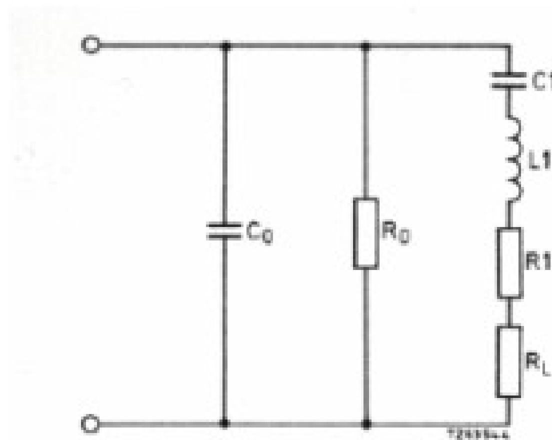

Figure 18 : Electrical equivalent circuit of a piezoelectric element.

In this model

R_1 is the resistance caused by mechanical losses.

R_L is the resistance due to radiated energy, $R_L=0$ in vacuum.

C_0 is the capacitance below the resonant frequency minus C_1 .

C_1 is the capacitance of the mechanical circuit.

L_1 is the inductance of the mechanical circuit.

The electromechanical coupling is modeled using a transformer as shown in figure *19*.

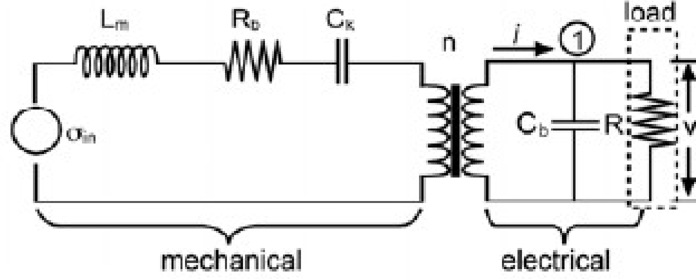

Figure 19 : Electrical circuit equivalent of a piezoelectric bender.

This representation is only valid if the excitation frequency is near resonance and the circuit parameters are constant independent of frequency.

Here

L_m represents the mass or inertia;

R_b represents the mechanical damping;

C_k represents the mechanical stiffness;

$\sigma_{in.}$ is an input stress generator;

C_b is the capacitance of the piezoelectric bender;

V is the generated voltage ;

n is the equivalent turns ratio of the transformer;

R is the external load which the generator will drive. The greatest power delivered to the load is when the load impedance matches the impedance of the source [*22*] . Impedances must be complex conjugates, resistances and reactances must be equal in amplitude.

The average power delivered to the load can be written as:

$$P_{rms}=\frac{V_{rms}^2}{R}=I_{rms}^2 R \tag{3.31}$$

Modeling of the optimal load resistance can be done by differentiating the equation of power with respect to the resistance, setting the result equal to zero and solving *for* R . The optimal load resistance for a *31* mode unimorph piezoelectric bender is given by:

$$R_{opt} = \frac{1}{(\omega C_b)} \frac{(2\xi)}{\sqrt{(4\xi^2 + k_{31}^4)}} \qquad (3.32)$$

Where ω is the driving frequency and ξ the damping ratio , k is the coupling coefficient.

However, because of the variations in material properties, the best way to determine the internal impedance of a power generator is by performing measurements on the device. This might be done after the processing of the device.

3.4 Power management circuit

3.4.1 Power generator as an integrated circuit.

An important aspect of the power generator is power management, there are several possibilities available for the composition of the device to ensure the most efficient energy generation [*23*]. Power management circuits will be addressed later but the integration of the circuit onto the same chip as the *MEMS* components is an important consideration. The power management circuit could be integrated on the same wafer as the *MEMS* structure or used as a discrete component.

The integration of *MEMS* and *CMOS* is a big challenge. As miniaturization is an important issue, the integration of the power management circuit is a big advantage. This integration offers a more practical and reliable solution for the final device. The investigation into this matter was made by consulting different manufacturing companies. *EuroPractice* offers a range of manufacturing possibilities through different *IC* companies, *MEMS* processing is however not available to date and is set to be available later this year. Processing of the *PZT* material is an other important constraint, *SINTEF* has successfully produced a power generator using the unimorph *31* configuration [*24*], the choice has fallen on this process to post-process the device.

3.4.2 External power management.

Due to the difficulty of integration of the electronic circuit on the same chip as the *MEMS* structure, it was decided to use an external power management circuit. The power management circuit plays an important role in the energy harvesting, power output can be managed efficiently and maximized.

The signal generated from the power generator is an AC signal which needs to be rectified. An amplifier can also be used in the form of a DC to DC converter. In addition some control logic may be integrated into the circuit in the form of a discharge circuit.
Figure *20* shows a block diagram of a simple energy harvesting circuit:

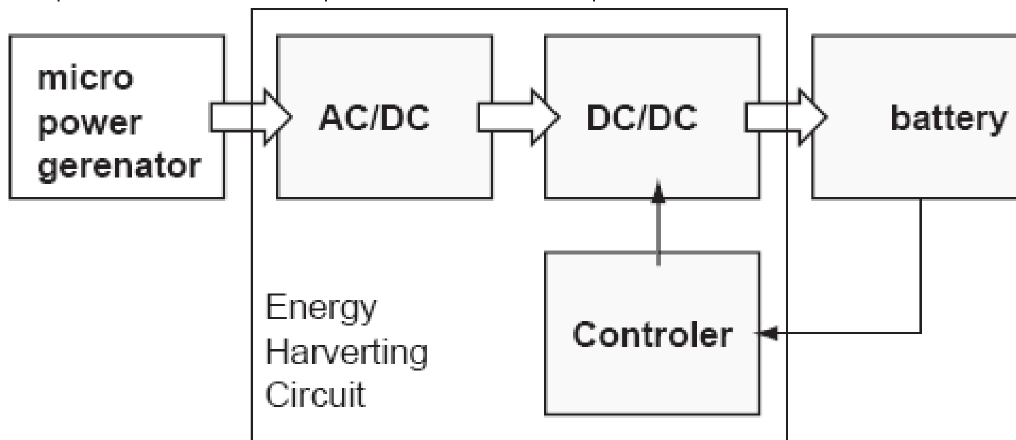

Figure 20 : Architecture of a power harvesting circuit.

A diode rectifier bridge can be used as a simple *AC*-to-*DC* converter. Assuming the voltage over the storage cell is constant and since the output of the *AC*-to-*DC* rectifier may vary, a *DC*-to-*DC* converter is used. This converter must induce as few losses as possible.
Figure *21* show an other possible configuration:

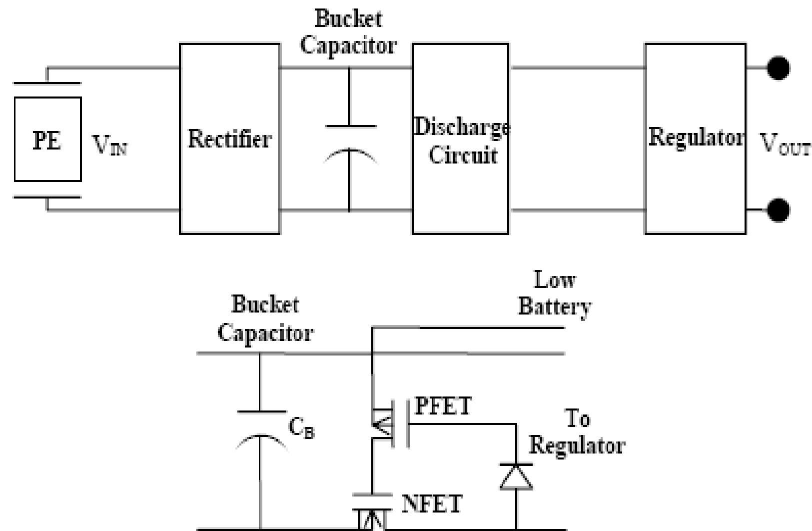

Figure 21 : Power management and discharge circuits of a power generator.

The charge in the bucket capacitor is discharged into the regulator when it is charged to a defined value. Low battery output falls low when the regulator output falls below a required level. This allows the capacitor to charge up again.

3.6 Conclusions

In this chapter, the modeling of the piezoelectric power generator was made using equivalent lumped models. From this model the importance of the resonance frequency was determine. Power is maximized if the cantilevers vibrate at the resonance frequency, power output is decreased by half if the deviation from the resonance frequency is 2% and is very small for more than 5% deviation from the resonance frequency.

Using the bending beam model and simulations, the effects of the variation of the beam dimensions on the frequency was determined. Thus for the choice of dimensions of the beams, long beams with small widths must be considered.

A mathematical modeling was done as well. Here the relationship between the dimensions and the electrical parameters was determined. Open circuit generated voltage and energy was modeled as well as the capacitance of the piezoelectric element. Simulations

were also performed on the generated voltage and total energy.

Finally, the piezoelectric power management circuit was addressed. Internal impedance was discussed. Thus to maximize the power output, load resistance must match the internal resistance of the piezoelectric element. Measurement is the best way to determine the internal impedance of the power generator. The choice was made to use a separate power management circuit because of the difficulty of integration of the circuit with the *MEMS* structure. The power management plays an important role in maximizing the power output. The AC signal from the power generator must be rectified using a *AC*-to-*DC* converter. A *DC*-to-*DC* converter is used to regulate and amplify the power output, and logic can be added to regulate the charge and discharge of the battery.

4 Design and simulations

4.1 Parametric study

In this section a parametric study is performed on the cantilever beam of the power generator, the aim is to determine the dimensions of the beams used in the power generator. First, the relationship between the different system parameters is developed. *3-D* models are developed in CoventorWare and *FEM* simulations are performed on different sets of beams. These simulations provide a more accurate resonance frequency than the previous method. Then after determining the range of dimensions used, an optimization is performed where saber simulations are performed. Saber simulations are fast and unlike *FEM* which require hours. Using this method, initial dimensions are determined and verified by *FEM* simulations.

Process limitations are then taken into consideration. The resulting dimensions from the FEM simulations are discussed and adjusted according to the design rules.

A second system is also introduced in this chapter. A biosensor is described and *FEM* simulations on the frequency and stress are performed. This device was introduced because of the similarities with the power generator and gain more insight on the designing using the *MultiMems*.

4.1.1 Process description:

The process used for the simulations was initially determined by the requirements of the system. However, after the choice of process, the *MultiMEMS* process was used for the simulations. This process similar to the one used earlier but does not include the *PZT* and the buffer layer. The *MultiMEMS* process is described in detail in chapter 5.

Layers used in the initial process are illustrated below:

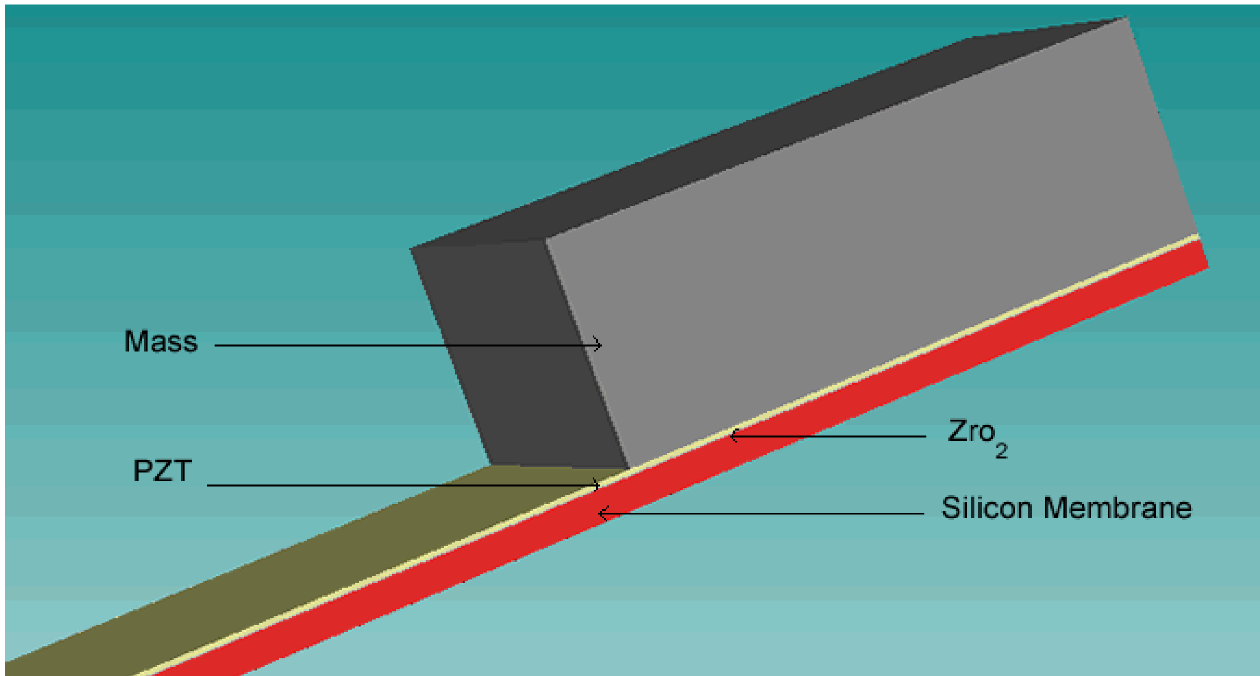

Figure 22: Layer description.

Epi : membrane, epitaxial layer of silicon beam.

ZrO_2 : buffer layer for the piezoelectric material.

PZT : Piezoelectric layer.

Mass : suspended mass at the tip of the beam, silicon.

As determined in chapter 2, *PZT* was chosen as the piezoelectric material due to its good properties. Table *8* shows some of the most important parameters used in the modeling of the system, these parameters are integrated in CoventorWare.

The membrane layer consists of an epitaxial layer of silicon, parameters and properties used for this material are described later in table *16.* these parameters are similar to parameters in the *MultiMems* process.

The thickness of the membrane and the suspended mass is determined by the *MultiMems* process.

ZrO_2 is the buffer layer which is needed to prevent reaction and interdiffusion between *PZT* and a thermally oxidized silicon. ZrO_2 has previously been shown to be a good buffer layer [*15*]. Parameters used for *Zirconia* are described in table *8*, and are gathered from various sources [*25*].

Thickness of the different layers are described in the table below:

Layer	*Description*	*Thickness*	*Units*
Si	Membrane	$2.8-3.3$	μm
ZrO_2	Buffer	0.05	μm
PZT	Piezoelectric layer	0.5	μm
$Mass$	Suspended Mass	23	μm

Table 7 : Layer thicknesses.

4.1.2 Material properties

The materials parameters used in the simulations are shown in the tables below:

PZT	
Parameter	**Specification**
Density $(kg/\mu m^3)$	$7.75\,10^{-15}$
Elastic constants E (MPa) Poisson ratio	$7.8\,10^4$ 0.28
Dielectric constant ϵ/ϵ_0	3800
Strain coefficient d_{31} $10^{-12}\,m/v$	320
Strain coefficient d_{33} $10^{-12}\,m/v$	650
Coupling coefficient k_{31} CV/Nm	0.44
Coupling coefficient k_{33} CV/Nm	0.75
Thickness	$0.5\,\mu m$
Zirconia	
Parameter	**Specification**
Density $(kg/\mu m^3)$	$6*10^{-15}$
Elastic constants E_1 Poisson ratio	$1.6\,10^5$ 0.27
Dielectric constant	20
Thickness	$0.05\,\mu m$

Table 8 : Piezoelectric and ZrO_2 parameters.

These parameters are introduced to the material file of *CoventorWare.* This material file contains the same parameters for the silicon as the file provided by *MultiMems*.

4.2.3 FEM simulations

Simulations based on the finite element method are performed in this section. These simulations are more accurate than the simulations performed earlier. Layout of the beam is performed and a *3*-D model is constructed.

First, a parametric study is performed to see the resulting resonance frequencies and determine initial dimensions, first the length of the beams are varied then a variation of the width was also performed. Variation of the length of the mass was performed next. The minimum allowed thickness of the *epi* layer is $3.2\mu m$ and is therefore not subject to any variation. Finally, The thickness of the piezoelectric layer was varied.

Variation of length of the beam

for these simulations, the width of the beam is set to $250\mu m$ and the length of the mass is held constant. The length of the beam is varied from 3.3 to $4.08\,mm$.
The resulting resonance frequencies are shown in the graph below:

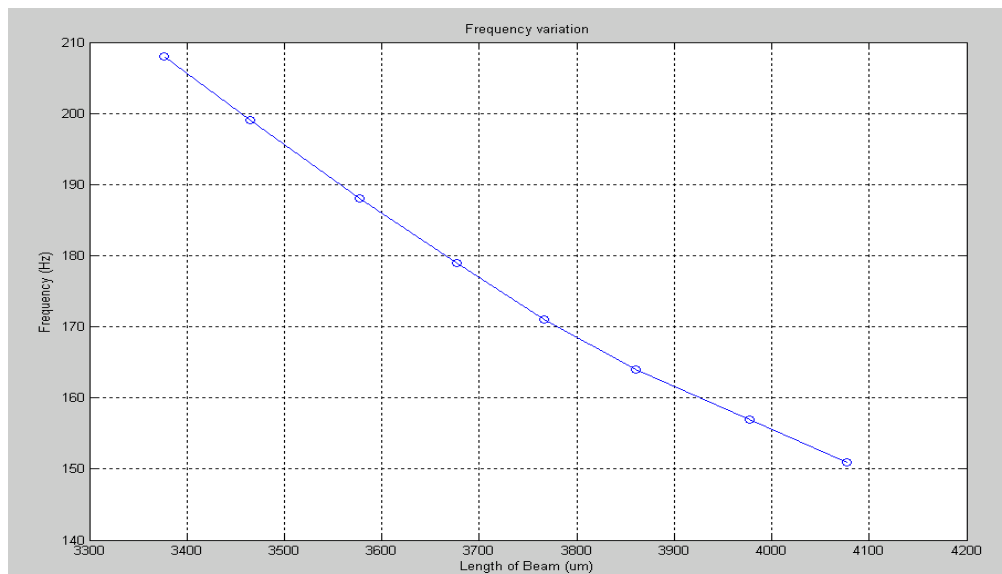

Figure 23 : CoventorWare simulations for different lengths of the beam.

The resonance frequency decreases with the increase of the length of the beam, as expected from earlier modeling. The fundamental frequency response for these simulations is in the range of 151 to $207\,Hz$. The stress levels are however close to $500\,Mpa$ and might not be possible to implement in practice.

Variation of the width of the beams

Resonance frequency is also affected by the variation of the width. The size of the mass and electrodes increases however with the increase of the width, to clearly see the effect of the variation of the width of the beam, the mass must be held constant. This is difficult to do in the *FEM* simulations but can easily done using Saber simulations.
In this section a few *FEM* simulations were performed on different beams with different widths. Table *11* shows the dimensions of the beams and the resulting resonance frequency.

Beam length	Beam width	Mass length	Frequency	Stress
4.1	200	450	172	390
4.1	210	450	167	390
4.1	220	450	168	390
4.1	230	455	160	400

Table 9 : Beam dimensions and the resulting frequencies and stress.

The length of the beam was held constant at $4.1\,mm$ and the width was varied by $10\,\mu m$ increments. The frequency decreases first with the increase of the width, then increases again. This is because of the increase in the mass, although the length is unaltered, a big variation of the size occurs because of the variation of the width. This decreases the frequency of the beam. The variation of the width alone tends to increase the frequency. This will become more evident in the Saber simulations.

Variation of the length of the mass

By varying the length of the mass, a change in the resonant frequency can be observed. L_m has been varied from $250-455\,\mu m$. The rest of the parameters are as follow: $L=4.1\,mm$, $W=250\,\mu m$, $W_e=190$.
Results are plotted in the figure below:

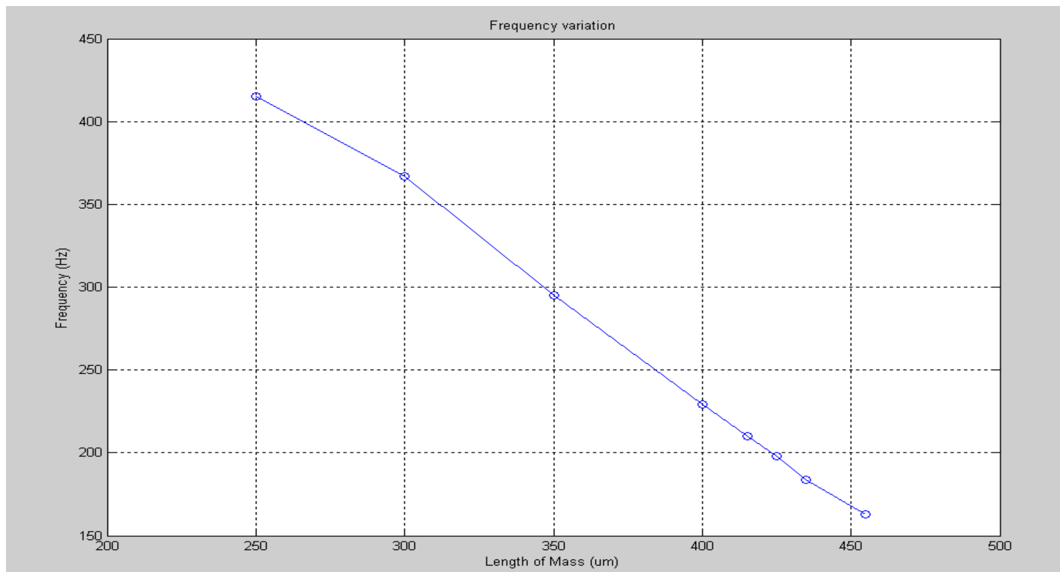

Figure 24 : CoventorWare simulations for frequency.

The lowest obtained frequency was $163\,Hz$ and a maximum stress of $390\,MPa$ was obtained. Further more the variation of the hight of the mass resulting in the following figure:

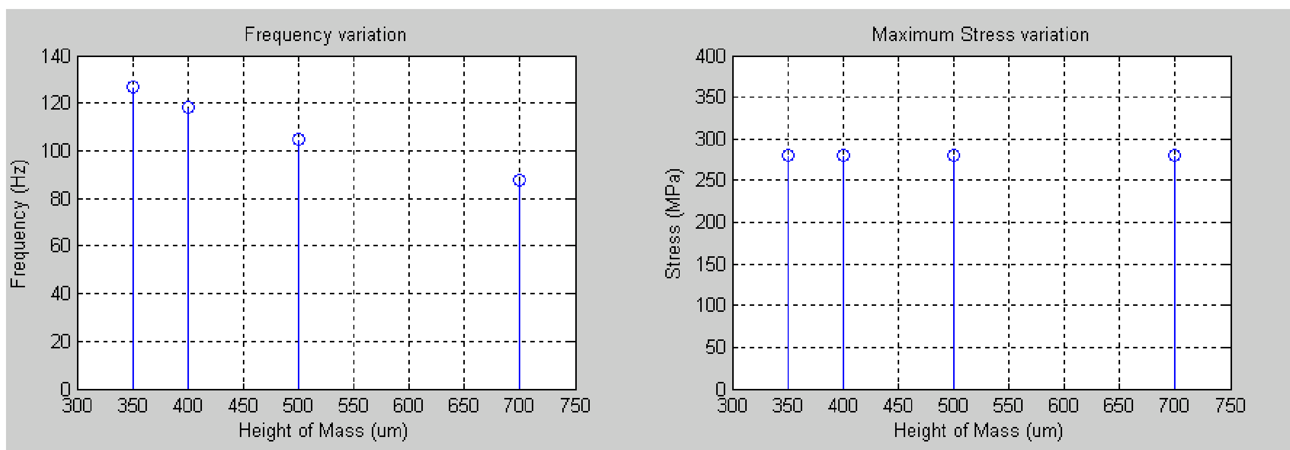

*Figure 25 : F*requency and stress plots for the variation of mass hight.

Variation of the height of the mass shows the same results as the variation of the length, the increase of mass height is however not possible in the MultiMems process, as maximum height is set to $23.1\,\mu m$. Figure *25* shows that it is possible to decrease the frequency below $100\,Hz$ for bigger masses.

4.3 Optimization of variables:

4.3.1 Geometrical beam dimensions: Saber simulations

An optimization of the design is performed in the Architect using CoventorWare, this function can perform parametric analysis of the design in a much faster way. The simulations are based on mathematical models and are made possible by combining macro models of known components in the Schematics environment. From the Architect, the layout of the design can be extracted, and a solid model can be constructed. A process is attached to the architect defining layers and their thickness.

A large set of simulations can be performed to optimize the design, mechanical simulations based on varying beam dimensions are performed. The optimization is based on determining the lowest resonant frequency.

Figure shows the schematics used in the design.

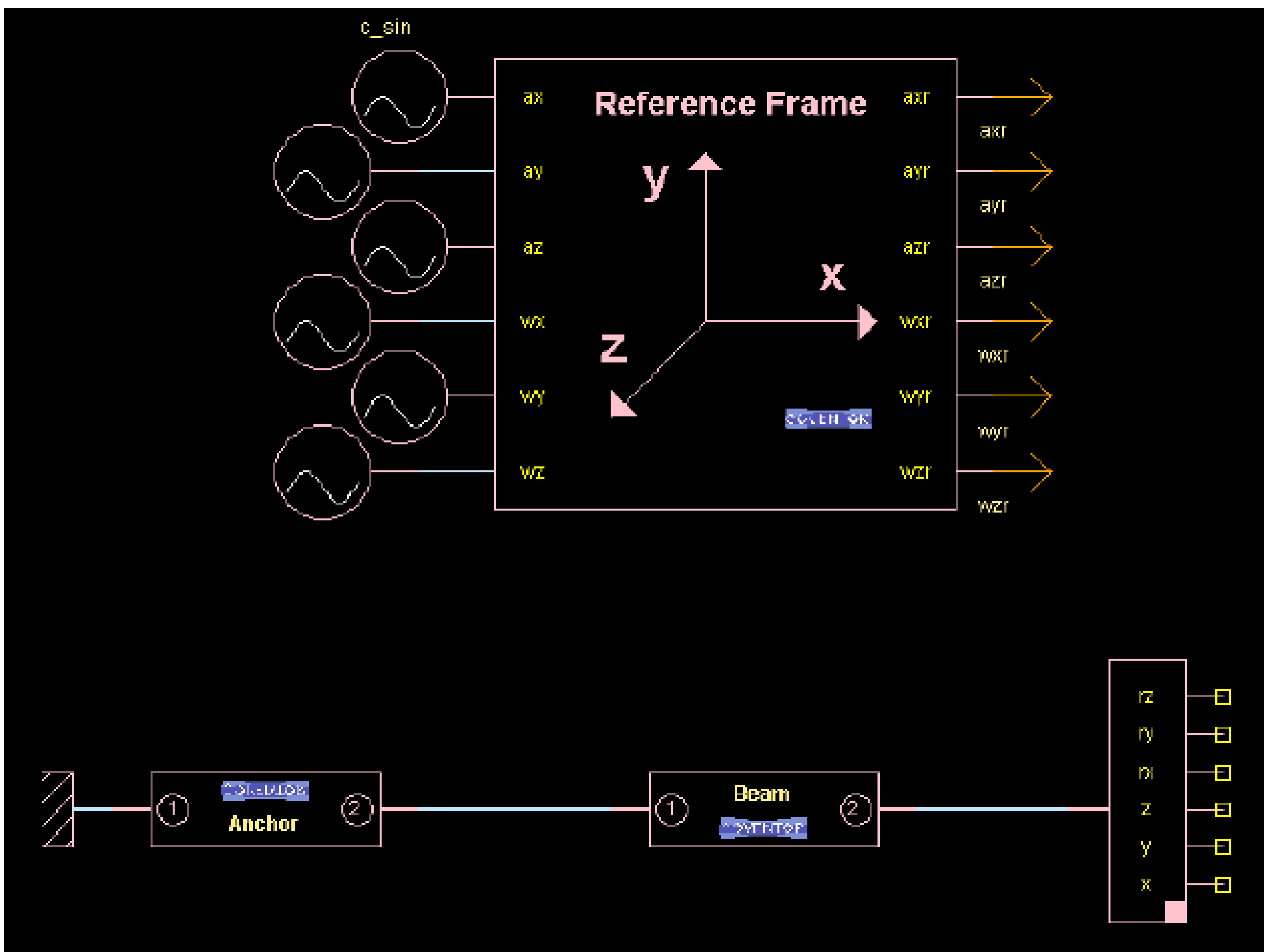

Figure 26 : Schematic setup.

The reference frame contains the anchor, beam and a mechanical connector. Each component has a set of properties defining position and dimensions, these must be carefully set. The suspended mass is defined within the beam. Many of the parameters can be declared as variables and are defined by using the *COVENTOR function*.

Layout extraction is performed and the 3-D model is verified. For more information on Saber Schematics refer to [26].

The initial parameters are listed in the table below:

Variable	***Description***	***Value***	***Units***
Mechanical variables			
L	Length of beam	4.1	mm
W	Width of beam	250	μm
L_m	Length of mass	400	μm
W_m	Width of mass	250	μm

Table 10 : Variables used in the simulations.

The variables are illustrated in figure :

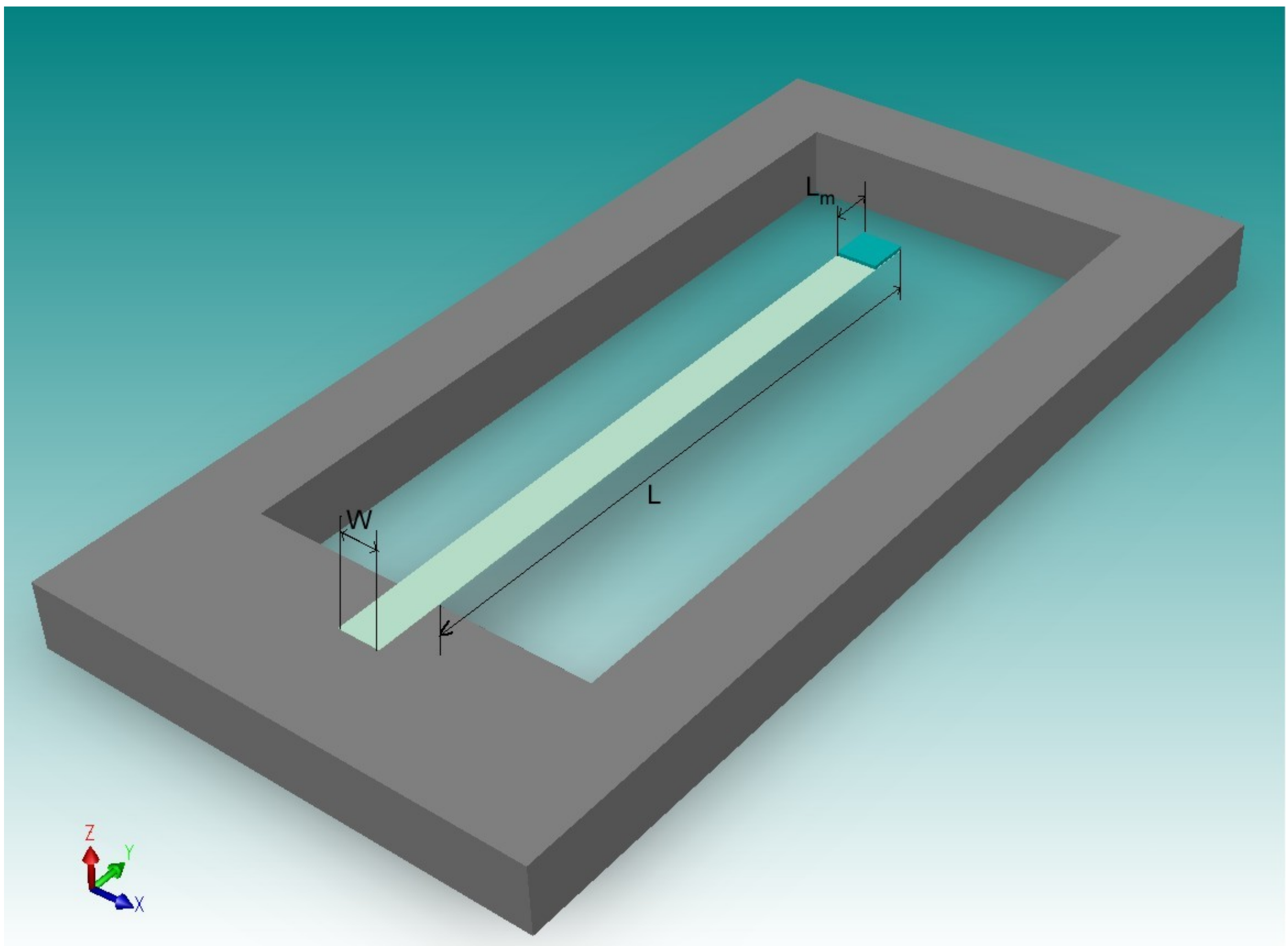

Figure 27 : Beam with suspended mass.

Modal analysis is performed on this beam where the length of the beam was varied from $3.1\,mm$ to $4.1\,mm$ with $100\,\mu m$ increments. The frequency response was plotted for each length.

The plot is shown in the figure below:

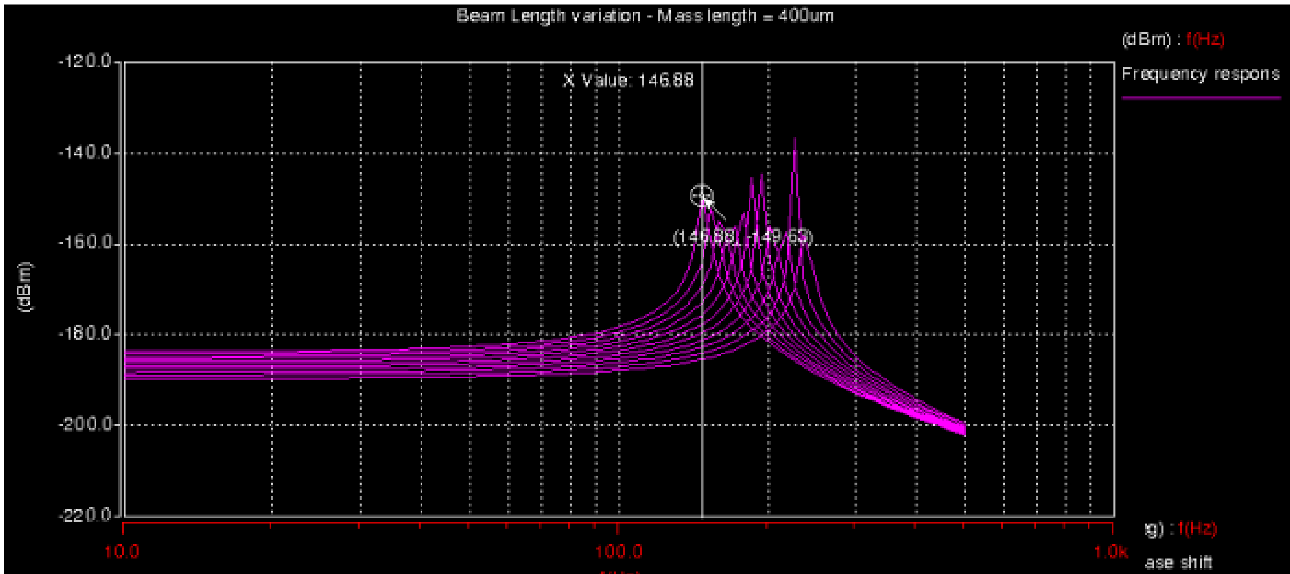

*Figure 28: F*requency response for the varying beam length.

The lowest frequency is obtain for the longest beam, $146.88\,Hz$. The frequency clearly decreases with the increase of the length of the beam. This is consistent with what was demonstrated by the *FEM* simulations.

A similar simulation was performed using the variation of the length of the suspended mass. The length of the mass was varied from 100 to $600\,\mu m$ with $50\,\mu m$ increments. The frequency response was plotted for each length.

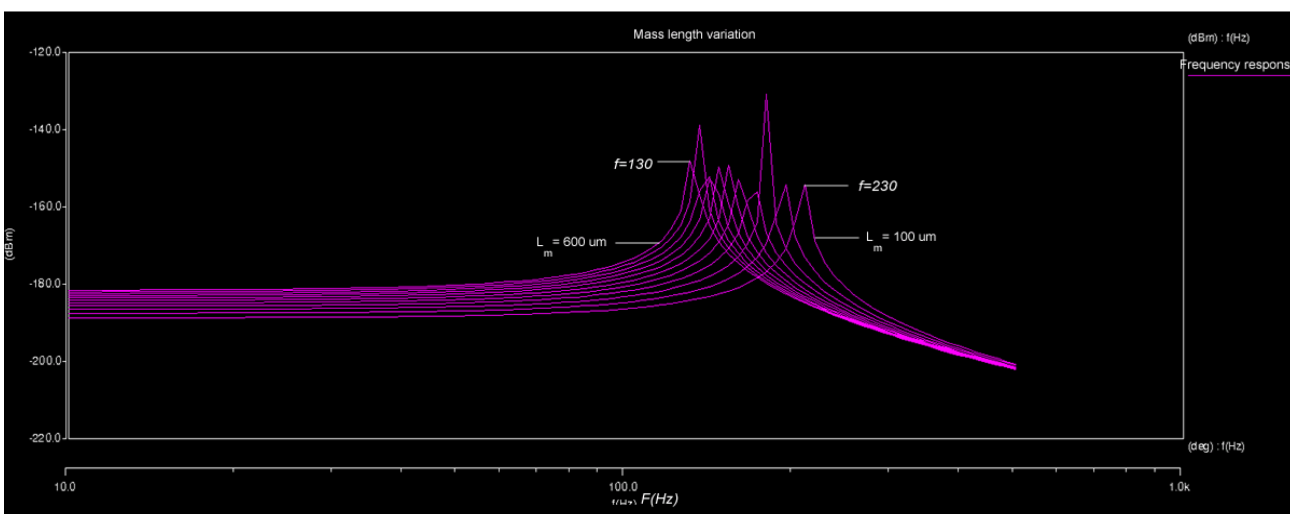

Figure 29: Frequency response for the varying mass length.

The lowest frequency is obtain for the longest mass, a mass length of $600\,\mu m$ results in a resonance frequency of $130\,Hz$, the decrease of the mass length results in the increase of the frequency. The upper frequency of $230\,Hz$ was obtain with a mass length of $100\,\mu m.$. The peaks in the figure show the maximum response to the excitation.

In an other simulation the width of the mass was varied beyond the width of the beam. The figure shows the variation of W_m from $200-400\,\mu m$.

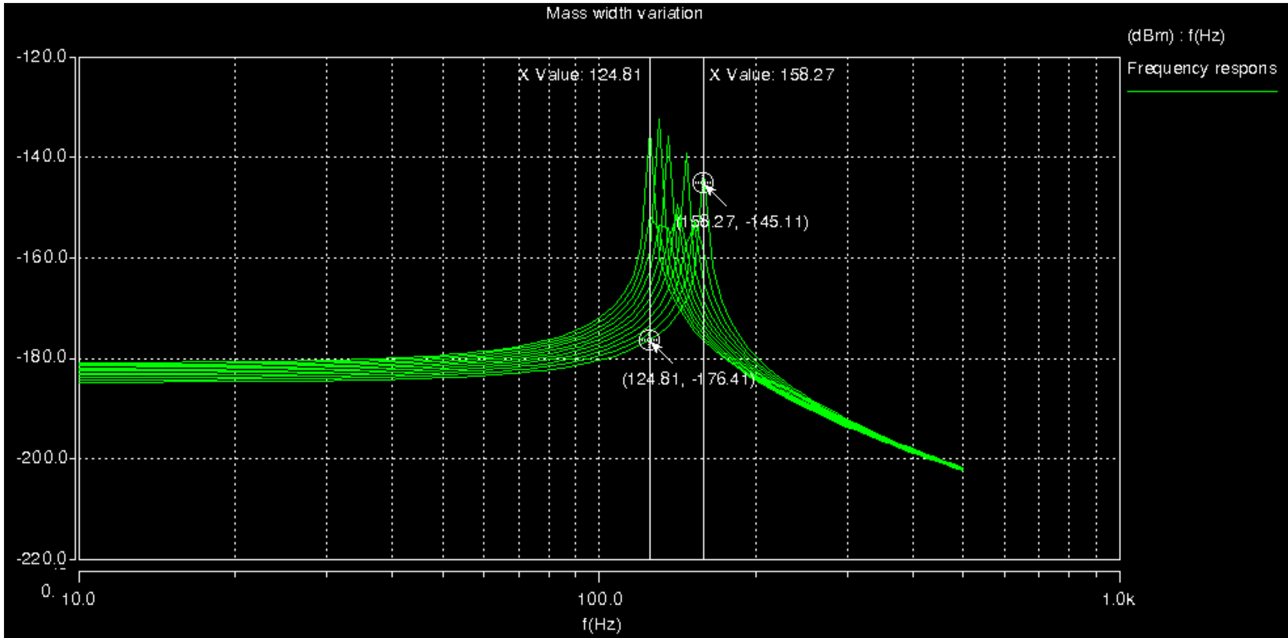

Figure 30: Frequency response for the varying mass width.

The simulations result in a frequency variation of $124\,Hz$ to $160\,Hz$.

These simulations can be combined into one set. This was done by varying the mass length and width, and simulating for each dimension. The results are shown in the figure below:

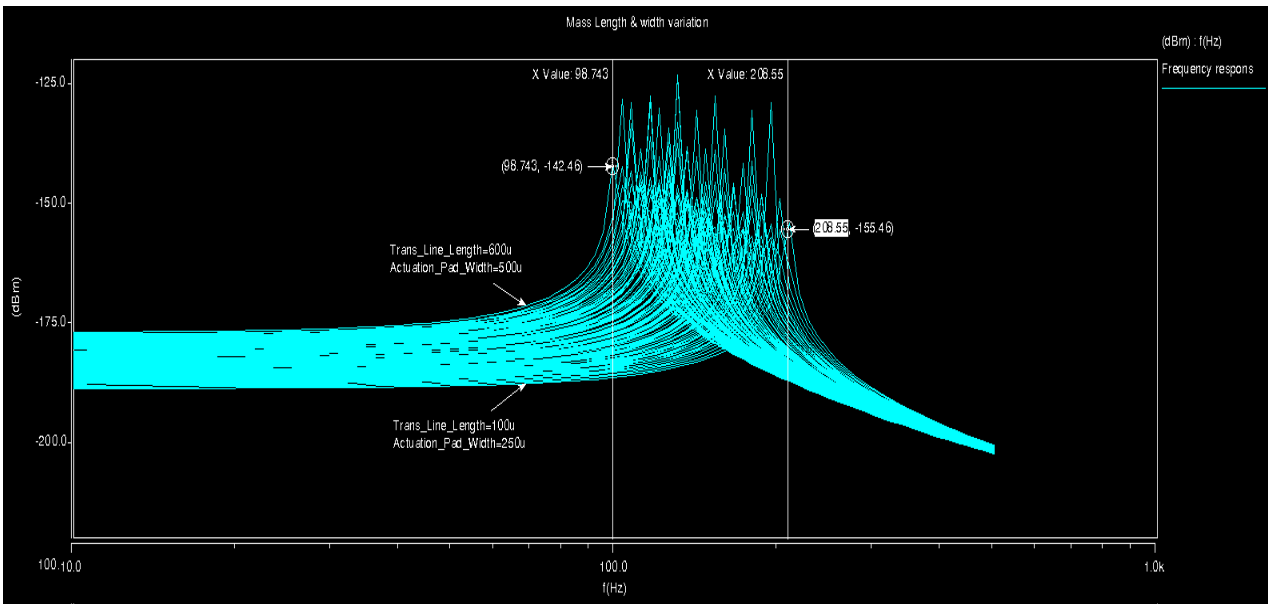

Figure 31 : Frequency response for the variation of mass length & mass width.

Here L_m is varied from 100 to 600μm with 50μm increments. And W_m was varied from 250 to 500 with 25μm increments. The resulting resonance frequencies range from 98.7 to 208Hz .

The smallest frequency resulted from the longest and widest mass.

The width of the beam was also varied from 200 to 400μm . The results are shown below.

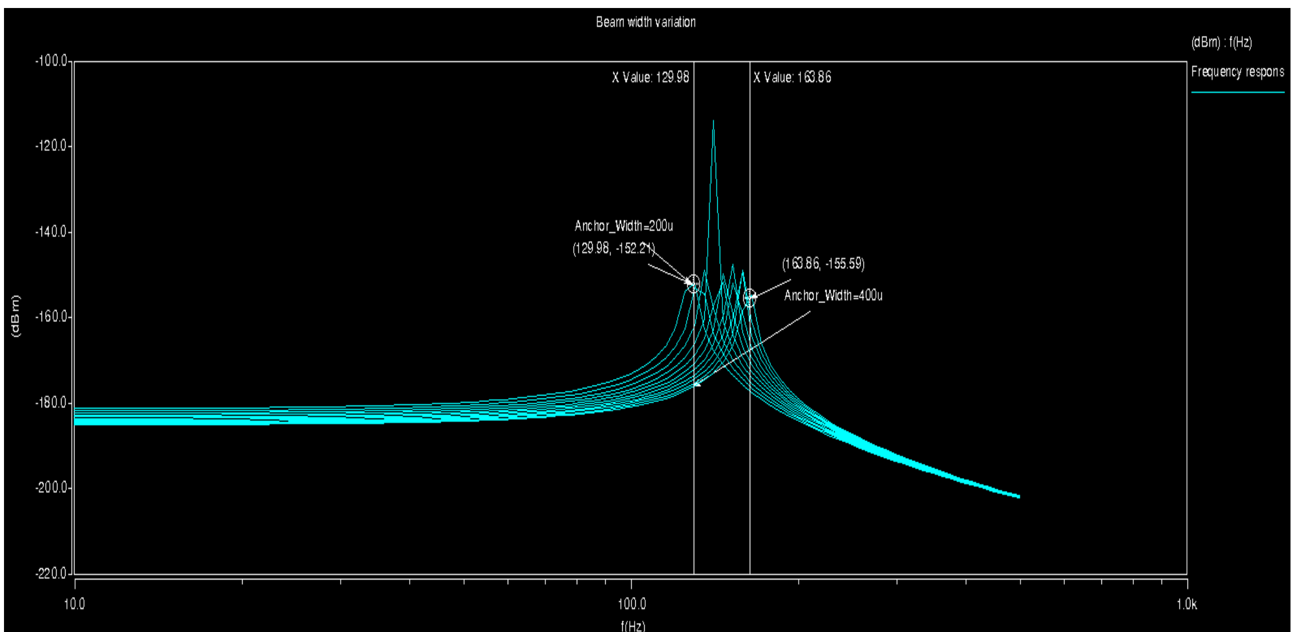

Figure 32 : Frequency response for the varying beam width.

The frequency range is 130 to 164 Hz in this case. The mass is held constant at 400μm and the width was varied in 20μm increments. This clearly shows an increase

in frequency with the increase of width of the beam.

4.1.3 Electrodes length and finger spacing

Power produced by the *PZT* is directly related to the strain of the beam.
Since the largest strain occurs at the clamped edge of the cantilever beam, the interdigitated electrodes should be placed closest to the clamped end where large strains are experienced.

Interdigitated electrodes are used to convert *31*-polarization to *33*-polarization as well as to generate the electrical energy. Therefore finger spacing and electrode width must be considered.

Figure 33 shows the relationship between the generated voltage and finger spacing.

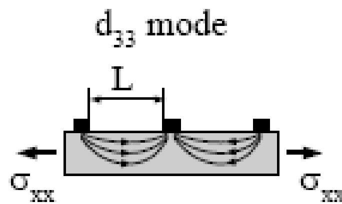

Figure 33 : Beam with interdigitated electrodes.

$$V_{33}=\sigma_{xx} L g_{33}$$

V_{33} is the open circuit voltage and *L* is the spacing between the electrodes. The generated voltage is much lager in the *33* mode since $g_{33}>2 g_{31}$ and *L* can be independently long ~ $10 * t_{pzt}$.

For the bending beam model, it was found that *PZT*, interdigitated electrodes with minimum electrode spacing concentrated on the clamped end of the beam offered the best results. Figure *34* below shows the IDT electrodes.

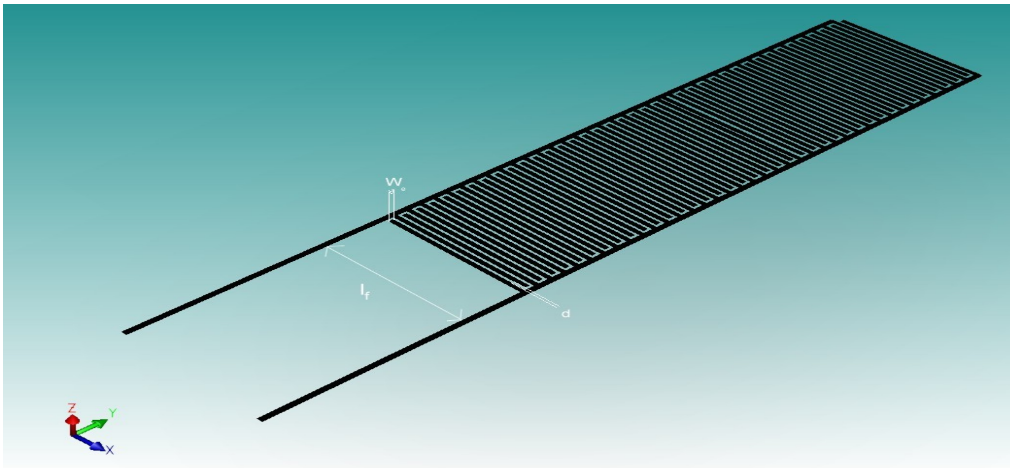

Figure 34 : IDT electrodes.

W_e is the width of the electrode, l_f is the length of the fingers. d is the spacing between the fingers.

4.3.3 Process limitations

According to the *MultiMems* process a set of conditions must be met in order to ensure that wafers can withstand the forces experienced during processing. An important condition is that the structure is able to withstand a 0.8 bar pressure difference between the two sides of a membrane with a through etch. This means that the beams must withstand a load of $0.08\,MPa$.

The optimal finger spacing for this design is $6\,\mu m$ with a finger width of $3\,\mu m$, this is however not possible to achieve in the *MultiMems* process. A minimum spacing of $20\,\mu m$ is required between conductors, also the conductor width can not be below $20\,\mu m$.

The issue must then be addressed as to the voltage necessary to establish an electric field which can penetrate the entire depth of the piezoelectric layer. The design rules for the electrodes must be broken in order to realize a structure with the a minimum spacing. $10\,\mu m$ was used for the spacing and width of the electrodes resulting in an under-etching of the electrodes of about $5\,\mu m$, the assumption is then made that the resulting spacing and width would be $5\,\mu m$. This was accepted by *Sensonor* after the submission of the design. The material use for the *IDT* electrodes is gold and is to be deposited *at SINTEF.*

4.3 Choice of dimensions

For the lowest frequency to be obtained the choice of the longest beam with a small width, as well as the biggest possible mass must be considered. The simulations performed in this chapter provide a basis for the choice of dimensions for each beam used in the generator. The choice of dimensions depends however also on process considerations and parameters.

In the simulations, the beams were subjected to a $0.001 MPa$ load, and the height of the mass was limited to $23 \mu m$. Provided these conditions, an initial choice of dimensions was made in order to meet the frequency and stress requirement :

Beam 1 : $L=4077 \mu m$ resulting in a resonant frequency of $f=151 Hz$.
Beam 2 : $L=3770 \mu m$ resulting in a resonant frequency of $f=170 Hz$.
Beam 3 : $L=3550 \mu m$ resulting in a resonant frequency of $f=190 Hz$.
Beam 4 : $L=3360 \mu m$ resulting in a resonant frequency of $f=210 Hz$.

The etched cavity has a width of $382 \mu m$ giving a width of $250 \mu m$ to the beam, the size of the mass is the same in each case: $L_m=436 \mu m$, and the width is $W_m=204 \mu m$. Stress levels are below $500\ MPa$

The *MultiMems* process imposes however a higher constraint on the load applied to the beams. Structures must withstand at least 0.8 bar pressure due to the process handling. After a large set of simulations it was determined that none of the beams would withstand such a load. Stress levels obtained using this load yielded about $3000*10^6 N/m^2$. New dimensions are therefore considered in this case. This will affect the resonant frequency which will increase considerably.

A new set of dimensions was determined according to the absolute design rules, these dimensions are listed below

	Length	Width	Mass $L \, x \, W$
Cantilever 1	1000	300	$291 \, x \, 236$
Cantilever 2	1000	300	$291 \, x \, 236$
Cantilever 3	809	100	$168 \, x \, 36$
Cantilever 4	500	100	$168 \, x \, 36$

Table 11 : Dimensions of the cantilevers.

The width of the mass takes into consideration the minimum required spacing between the epi layer and the release etch mask.

Modal analysis is performed on the beams, the resulting resonance frequencies are presented below:

	Frequency
Cantilever 2	$1.894 \, kHz$
Cantilever 3	$3.362 \, kHz$
Cantilever 4	$8.5322 \, kHz$

Table 12 : Resonance frequencies of the cantilevers.

The resulting resonance frequencies are very high compared to the initial design, but can still be used considering the process.

Both the initial and alternate designs were submitted to Sensonor. A decision was made not to go through with the processing of the first design because of the risks involved. Additional costs would be imposed and production downtime would result in case of structure failure.

4.4 Cantilevers for microBUILDER tester

4.4.1 Design and specifications

An additional design was done in this work using the same *MultiMems* process. This design was requested by *SINTEF* and consists of a set of cantilevers with piezoresistive bridges used for biomolecular detection. The device is a biosensor and will be used as part of a *microBUILDER* tester.

Similar devices have been developed by *IBM* and *Cantion* [27] and the aim here is to construct longer cantilevers for optical readout of the deflection.

Figure *35* below shows the basic structure of each beam:

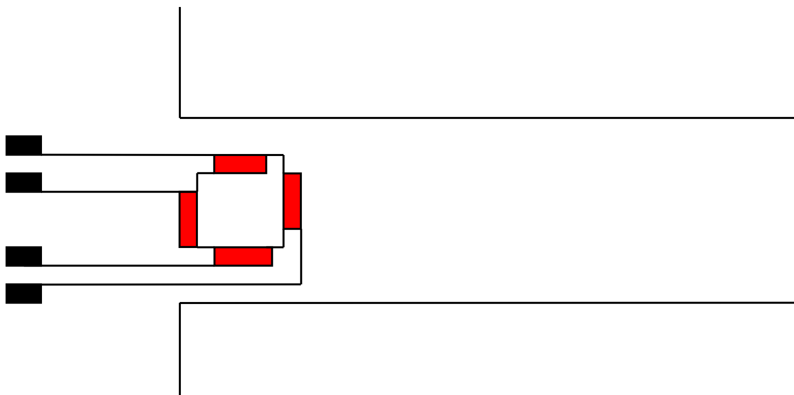

Figure 35 : Cantilever with piezoresistive bridge.

Specifications of the device were discussed with *SINTEF.* Die size used is $6 \times 6\, mm^2$ with 4 aluminum bond pads and 4 conductors for each cantilever.

Beam dimensions are listed in the table below:

	Cantilever 1	Cantilever 2
Cantilever thickness	$3.2\,\mu m$	$3.2\,\mu m$
Length	$700\,\mu m$	$1000\,\mu m$.
Width	$150\,\mu m$	$300\,\mu m$.

Table 13 : Cantilever dimensions.

Resulting resonance frequencies for the cantilevers are:

- $8.86\,kHz$ for cantilever 1 .
- $4.30\,kHz$ for cantilever 2.

Stress levels are at $430\,Mpa$.

The piezoresistive bridge consists of 4 equal piezoresistors with a resistance of $2\,k\Omega$. The corresponding dimensions for the piezoresistors are $15\,\mu m$ long and $5\,\mu m$ wide.
Surface and buried conductors are to be used on the cantilevers, metal conductors are only used in the pads area outside the glass cavity. Surface conductors width is set to a minimum of $20\,\mu m$ for good conductivity.

Absolute design rules must be considered in the layout of the design, the positioning of the piezoresistive bridge will depend on these rules. The number and placement of the cantilevers is determined by these design rules.

This design was added to the project because of the similarities with the power generators design and to gain a more insight in the designing procedure using the *MultiMems* process. Layout and processing is addressed in the next chapter.

5 Processing & Layout

5.1 Process description

Low cost prototyping and limited volume production are possible with Multi Project Wafer *MPW* services in which devices of different customers are fabricated in a single wafer run. Since multiple customers share the same mask set, the costs of mask making and fabrication are divided. The companies considered for the processing are *Infineon Technologies SensoNor* and *Tronics Microsystems* which both offer multi-project wafer processing.

Tronics Microsystems [*28*] fabrication process is a *DRIE* High Aspect Ratio Micromachining on $60\,\mu m$ thick SOI (Silicon-on-Insulator) substrate featuring a hermetic silicon wafer level package. Through this approach, it is possible to design highly sensitive capacitive transducers, electrostatic actuators, resonators and energy scavengers. This process is however not suitable for the power generator since the resulting beam would have a thickness of $60\,\mu m$.

Infineon Technologies SensoNor As [*29*] has leading expertise in the development and design of Micro Electro Mechanical Systems. The company has its own wafer fabrication facility, as well as high-volume back-end production and test facilities.

SensoNor's bulk micromachining multi-project wafer process offers the fabrication of buried and surface piezoresistive sensors, thin silicon diaphragms and masses, cantilevers and channels as well as glass and silicon cavities in a triple-stack anodic bonded configuration. Previously fabricated microsystems which are representative of the capabilities of this process include: absolute and differential pressure sensors, microfluidic flow sensors, accelerometers, and force sensors.

Processing of the piezoelectric materials is however not possible at either companies, only through *SINTEF* can this be achieved. *SINTEF* is the largest independent research institute in Scandinavia. The Department of Microsystems and Nanotechnology has performed numerous studies and designed various microdevices. *SINTEF* has its own clean

room manufacturing line. The post-processing of the power generator is to be performed at *SINTEF.*

Throughout this chapter, the layout and processing of the power generator and the biosensor using the *MultiMems* process is addressed. Cantilever dimensions for both designs were determined in the previous section. The dimensions are verified here using the design rules of the *MultiMems* design handbook [30].

5.1.1 *MultiMEMS MPW* process

The *MultiMEMS MPW* process is based on SensoNor's well-established bulk silicon and glass micromachining technologies. This process is well suited for the design of the cantilever structures needed for the power generator and the biosensor.

Figure 36 shows a cross section of the complete process.

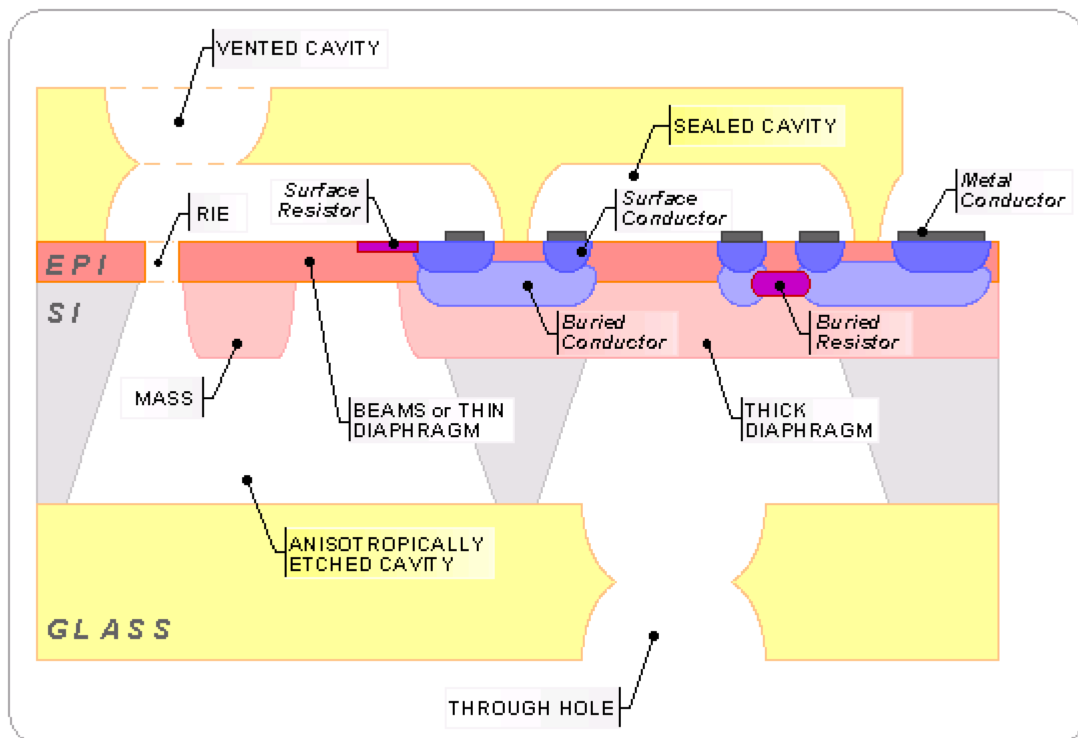

Figure 36: Cross section of the *MultiMEMS* technology showing its main features .

The following main features are considered essential in both designs.

- High aspect ratio front-side etching with *RIE* enabling production of free-standing masses.
- Highly sensitive surface piezoresistors, for thin membranes.
- Triple-stack glass/silicon/glass anodic bonding.
- Hermetically sealed cavity structures with electrical feed-through.
- Membranes and masses are limited to $3\,\mu m$ and $23\,\mu m$ values.

The design handbook gives a more detailed presentation of the process.

There are two *MultiMEMS MPW* runs per year, run 10 is scheduled for April/Mai 2007 and is therefore chosen for the fabrication of the devices. The cost per project is $1500\,eur$ for academic users and is financed by *SINTEF*.

5.1.2 Process steps

The fabrication process considered here does not include deposition of the *PZT* and buffer layers. The fabrication flow is similar in both designs.

Table *14* presents the different steps involved in the fabrication process of both designs. Detailed description of the process is given in the design handbook.

Process step	**Layer**
• Thermal growth and patterning of oxide. Phosphorus implantation to define *n*-wells.	N-Well areas
• Boron implantation and thermal diffusion, to define *p*-type buried conductors.	Buried conductors*
• Growth of *n*-type epitaxial layer and removal of back surface oxide.	*Epi* layer
• Thermal growth of thick and thin oxide.	Thick and thin oxide
• Boron implantation and thermal diffusion, to define *p*-type surface conductors.	Surface conductors*
• Boron implantation and thermal diffusion, to define *p*-type surface resistors.	Surface resistors*
• Phosphorus implantation. The surface *n*+ layer forms ohmic contacts.	N+ areas
• Etching of contact holes in the thin oxide.	Contact holes

Process step	Layer
• Metal deposition, patterning and annealing, to form metal conductors.	Metal
• Patterning of back surface oxide. Anisotropic Wet etching of bulk silicon.	Back side etch
• Removal of back surface oxide. Patterning of front surface oxide to expose bare silicon in the anodic bonding areas.	AB areas
• Release of structures by RIE. Dry etching.	Release etch
• Wet, isotropic etching of glass to form cavities and throughholes. Removal of mask on both surfaces.	Top and bottom glass
• Triple-stack anodic bonding of the silicon and glass wafers.	
• Bridge sawing and wafer dicing.	

Table 14 : *MultiMems* process steps.

These steps are used in the design and simulation of the devices and are provided as a process file by *MultiMems*.

* steps performed for the biosensor only.

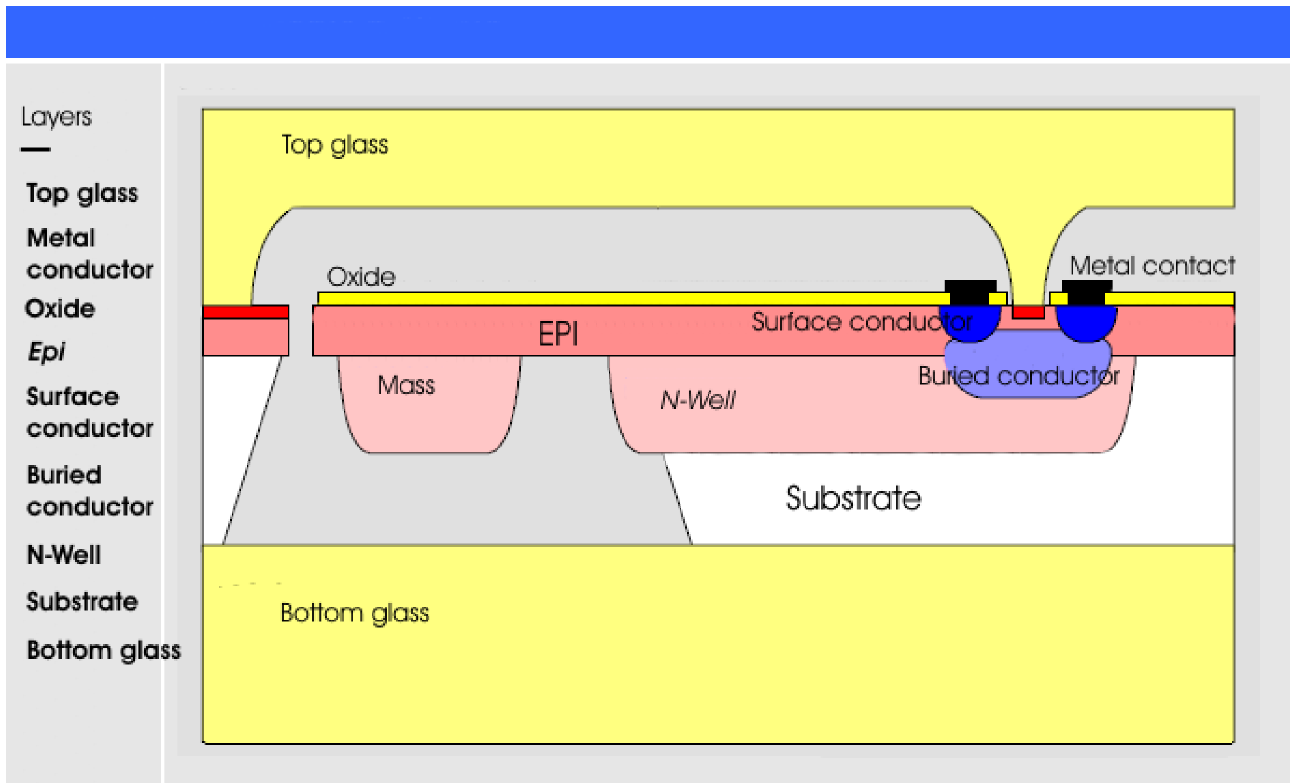

Figure 37 : Layers used in the power generator.

Figure *37* shows the different layers used in the fabrication process of the power generator. A cantilever is realized in the *epi* layer with a suspended mass in *N-well*. A thin layer of oxide covers the entire beam, buried and surface conductors are used to connect eventual electrodes with the pads. The entire device is hermetically sealed by a top and bottom glass layer.

The biosensor uses a similar configuration in addition to the piezoresistive bridge, constituted of buried conductors and piezoresistors.

5.1.3 Design specifications and considerations

Guidelines are provided here to the different design specifications and limitations, material characteristics and dimensions are discussed. Etching properties are addressed as well as die dimensions.

Materials

Material parameters are provides in the process file from *MultiMems* and the design handbook, relevant parameters are summarized in tables *15* and *16*.

Silicon substrate	
Parameter	**Specification**
Crystal orientation	(100)
Primary flat orientation	{110}
Density $(kg/\mu m^3)$	$2.331 * 10^{-15}$
Elastic constants E_1 Poisson ratio	$1.301\,10^5$ 0.278
Electrical conductivity $(pS/\mu m)$	$1.4 * 10^9$
Thickness	$2.20 \pm 0.07\,\mu m$
Specific resistivity	$3.0 \pm 0.6\,\Omega cm$

Table 15 : Material properties of the silicon substrate.

Epitaxial layer	
Parameter	**Specification**
Thickness	$2.20 \pm 0.07\, \mu m$
Specific resistivity	$0.11 \pm 0.01\, \Omega\, cm$

Table 16 : Material properties of the epitaxial layer.

Dimensions

An important design limitation is the thickness of membranes. Table *17* shows thickness of membranes realized in this process.

Membrane	Thickness μm
Thin membrane	3.1 ± 0.3
Thick membrane	23.1 ± 1.0

Table 17 : Membrane thicknesses.

Thickness of the cantilever beams are limited to $3.1 \pm 0.3\, \mu m$ and maximum thickness of the mass is $23.1 \pm 1.0\, \mu m$.

An other limitation imposed on the design is the maximum allowed width of membranes.

Membrane type	Max width square membranes W=L	Max width square membranes W=2*L
Thin	$W = 430\, \mu m$	$W = 340\, \mu m$
Thick	$W = 3480\, \mu m$	$W = 2790\, \mu m$

Table 18 : Maximum width of membranes.

These dimensions can withstand the absolute design limitations and can be used without further simulations. However, longer structures can still be achieved as long as they can withstand process handling. Structures can be subjected to 0.8 bar. Maximum stress in the material can not exceed $\sigma_{MAX} = 500\ MPa$.

Because of this limitation, the desired resonant frequencies can not be obtain for the power generator. Cantilever dimensions were regulated in the previous chapter to meet absolute design limitations.

The design handbook gives a detailed description of other material dimensions. Thickness of the different layers is described in detail but are not important for the design of neither devices.

Etching

Wet anisotropic etching of the silicon is subject to many considerations. The silicons primary flat orientation is <110> and the wafers plane is a <100> plane. The wet etching process results in an angle of 54.74^o between the <100> and <111> planes. This affects the size of cavities under the cantilevers, the number of cavities fitted in the die also depends on the size of the cavities.

This type of etching imposes a set of layout rules that must be respected, these rules are addressed later in this chapter.

The figure below shows the profile of the wet anisotropic etching.

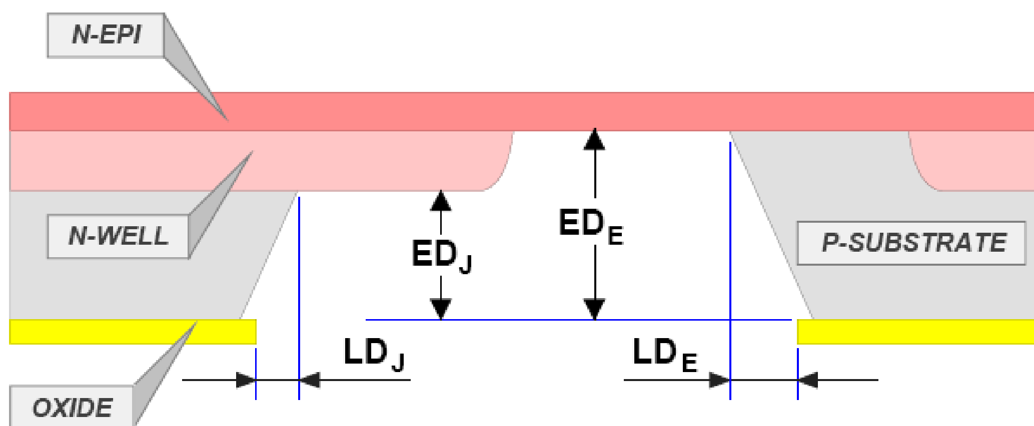

Figure 38 : Wet etching profile.

The wet etch results in an underetch that must be considered in the layout. This under etch limits the number of cavities in the die area. Underetching is addressed in detail in the design handbook.

The bulk silicon etching is performed in a tetramethyl ammonium hydroxide (*TMAH*) based solution, using silicon oxide as a mask. This etching is performed on a two-level *pn*-junction. Etch stop is achieved by employing a reversed bias to the *pn*-junction. Due to the electrochemistry of the process, silicon etching is stopped when the passivation potential is exceeded enabling an effective control of the depth of the etching. This etch will however result in a transition region between the epi layer and the *N-well* region. The profile of this transition region is shown in figure *39*.

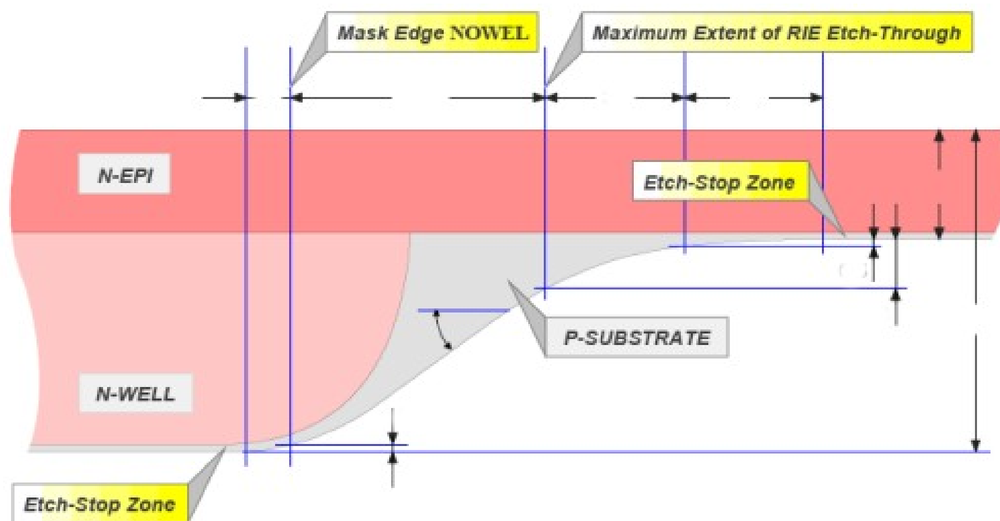

Figure 39 : Profile of the transition region.

This transition region may affect the characteristic performance of the cantilevers. Further study is needed to account for these effects.

Die dimensions

Die size used for the power generator and the biosensor is $6x6mm^2$. The choice of die size was made according to the initial dimensions of the power generator, however these dimensions could not be processed using the *MultiMems* process. The decision was made to keep the chosen die size. For the biosensor, *SINTEF's* specifications require the use of a $6x6mm^2$ die.

Figure *40* shows the configuration of the die.

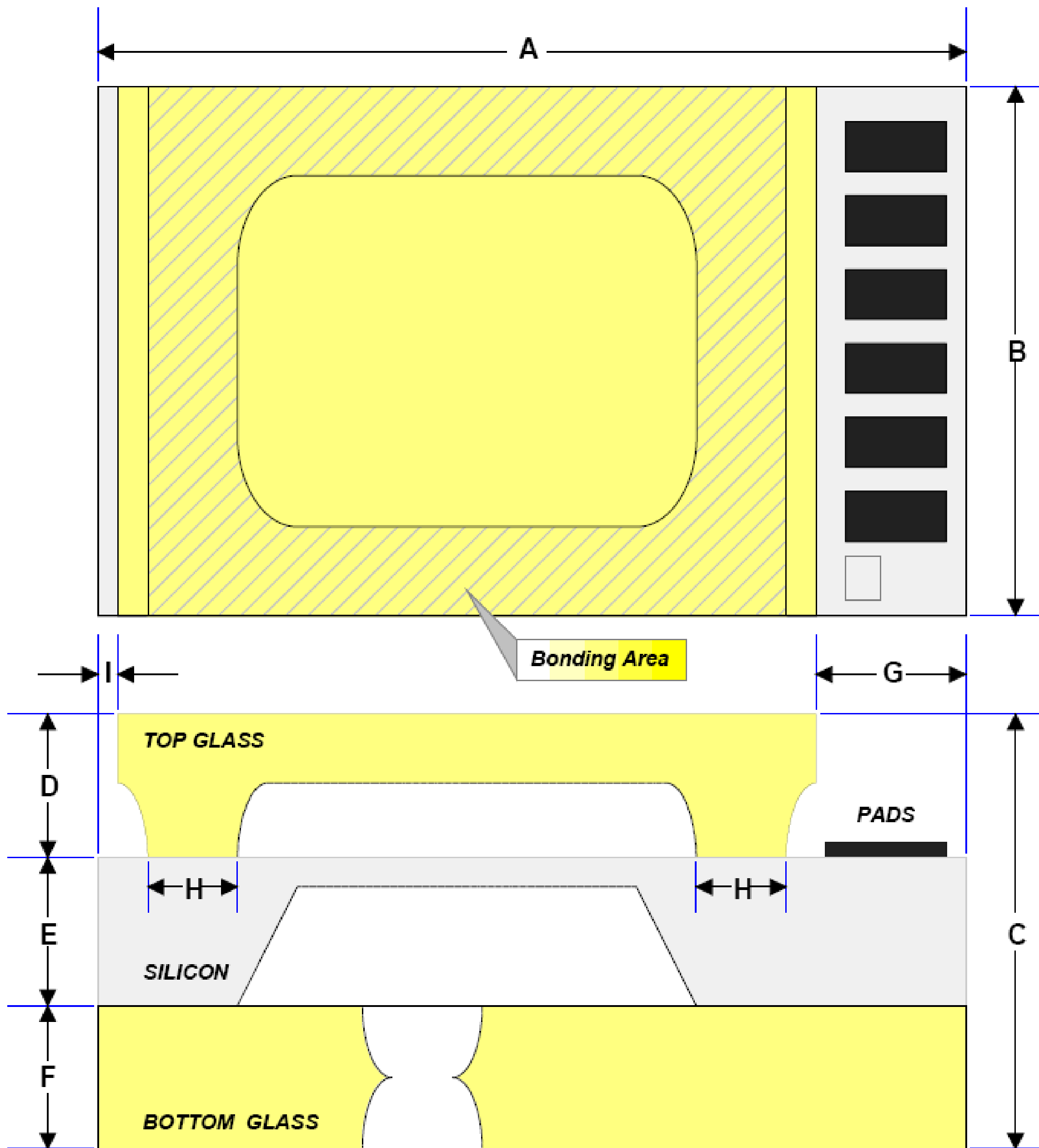

*Figure 40 :*Top and side view of the *MultiMems* die.

Size specifications of the different dimensions are given in detail in the design handbook. The width of the pads and the bonding area is particularly important. The number of beams depends on the available area inside the glass cavity.

For the power generator to generate maximum power, maximum number of cantilevers must be used. It is also desired to have several beams in the biosensor in order to compare the performance of the different beams.

In the case of the power generator, the number of beams is limited by the size of the

cavities. Each cantilever has its own cavity and the distance between cavities must be respected. For the biosensor which require 4 pads per beam, the number of beams is limited by the spacing between the pads and the spacing between the cavities.

An effective area can be determined for the fitting of the beams within the die. Details about dimensions are addressed in the design rule section.

5.2 Design rules

The available space of the design is determined by the layout rules. Process steps and considerations such as the wet or dry etching impose a set of absolute layout rules that must be respected. The use of the different conductors and pads is also regulated by layout rules. Layout rules are presented in the design handbook.

Taking into account the layout rules for the different layers, dimensions of both systems are determined. Templates are used for the predefined components, these templates include templates for the different pads, die outline, buried feed through and a set of assist cells.

5.2.1 Mask set

Mask names and polarity are used as indicated in the design handbook. Assist masks are used in addition to the masks illustrated in figure *41* below:

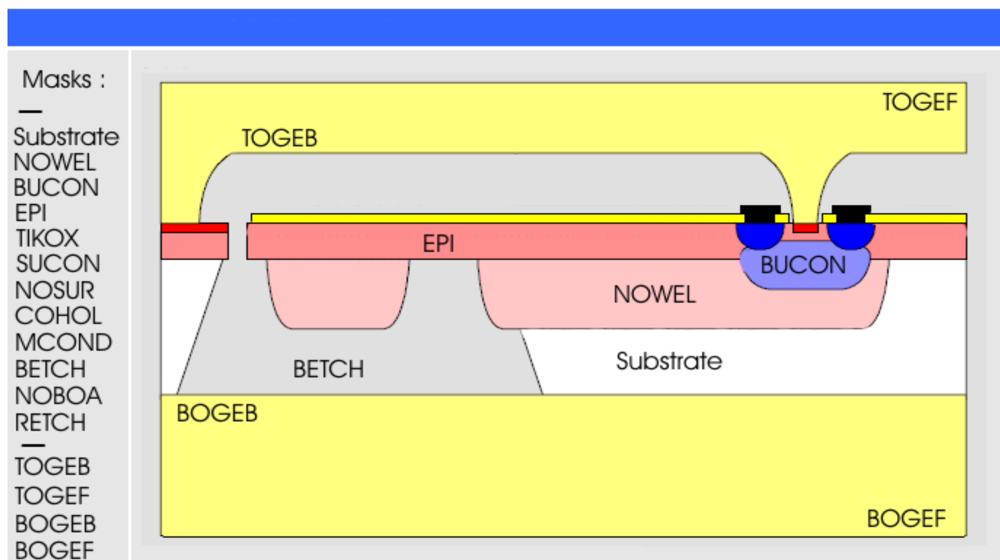

Figure 41 : Mask set used in the layout.

5.2.2 Power generator layout

For the power generator the layout results in 4 cavities with 2 pads per beam. The minimum distance between the cavities is $311\mu m$ and the spacing between the pads is set to $123\mu m$. Cantilever dimensions are shown in the table below.

	Length	Width	Mass ***L x W***
Cantilever 1	1000	300	328 x 273
Cantilever 2	1000	300	328 x 273
Cantilever 3	809	100	205 x 73
Cantilever 4	500	100	205 x 73

Table 19 : Beam dimensions.

The complete set of dimensions for the entire system is provided in the appendix.

Standard wire bond pads are used to provide electrical contact to the *die*'s p-substrate. *Epi* wire bond pads provide electrical contact to the *epi* layer. These pads must be connected to the ground in order to avoid electrical leakage currents and undefined potentials.

The layout is organized in cells defining the hierarchy of the design. The top cell containing beam cells which contain buried feed through and pads.
CoventorWare is used for the layout.

Figure *42* shows the layout of the power generator. Interdigitated electrodes are included in this layout, assist layers show the actual glass cavity and the cavity in the silicon substrate. Buried conductors are used for the feed trough.

Spacing between the metal conductors is $10\mu m$ which is a violation of the design rules. This was considered as discussed earlier.

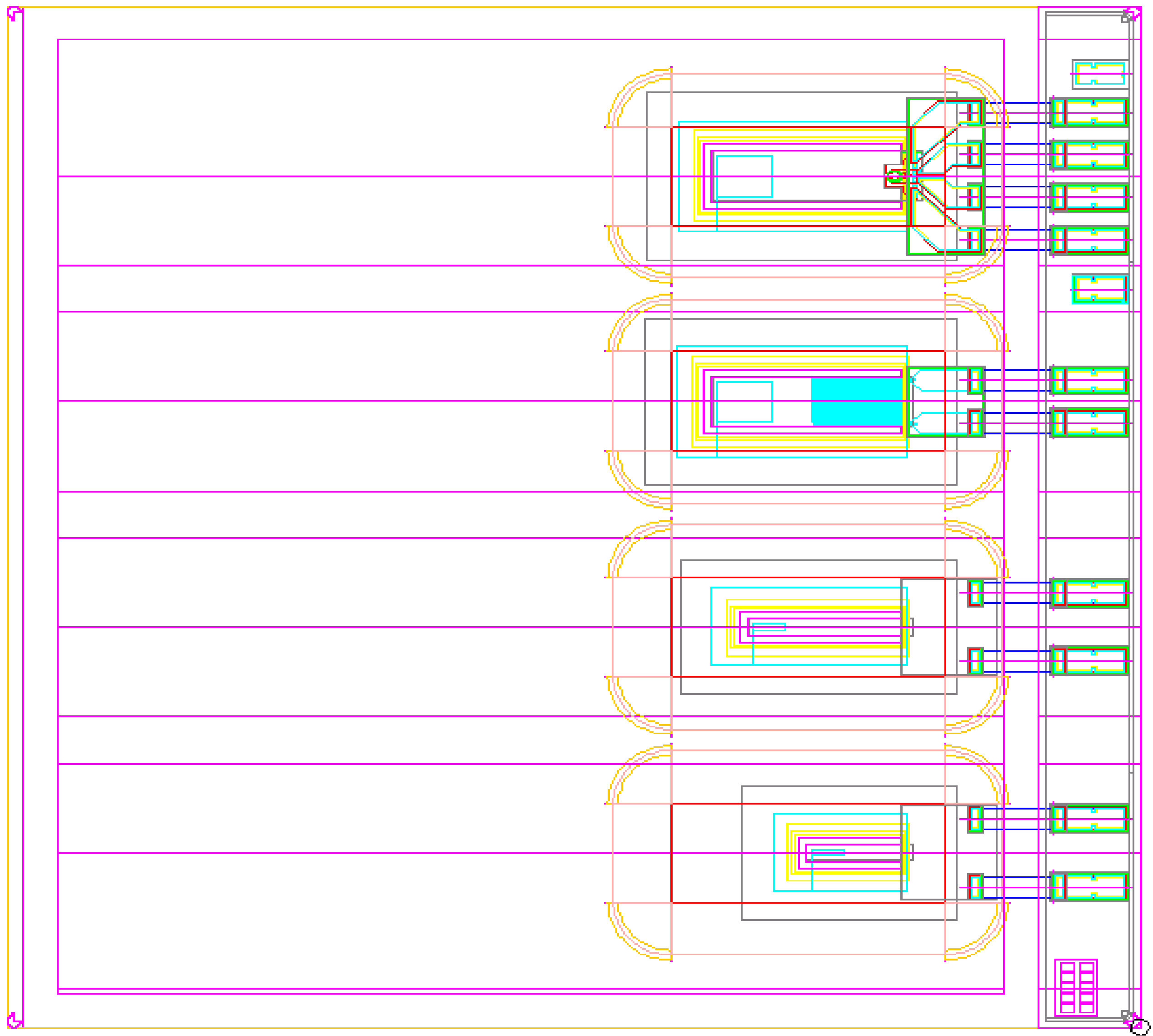

Figure 42 : Layout of the power generator.

The layout is composed of 4 beam cells, one with interdigitated electrodes, one with a piezoresistive bridge and two cantilevers with a suspended mass. The design was changed in the last minute. This is because of process incompatibilities between *SensoNor* and *SINTEF.* This made the post processing of the *PZT* material impossible.

5.2.3 Acceleration sensor layout

Considering the layout rules for the biosensor, 4 cavities are used with 4 pads for each cantilever. The spacing between cavities is $375\mu m$ and $120\mu m$ for the pads. Different piezoresistive bridges were designed for each cantilever. Table *20* shows the different beam dimensions with their respective piezoresistive bridges.

	Length	Width
Cantilever 1	1000	300
Cantilever 2	1000	300
Cantilever 3	716	150
Cantilever 4	716	150

Table 20 : Beam dimensions for the biosensor.

Dimensions of the piezoresistors were kept constant. A figure showing all the related dimensions is given in the appendix.

Figure *43* shows the layout of the biosensor. The complete set of masks used in the layout is shows in figure *41*, assist layers are used to define actual cavities and symmetries. This cell contains the piezoresistive bridge and the pads. Buried conductors are used for the feed trough, and surface conductors connect the bridge to the pads according to the specifications.

Standard wire bond pads and *Epi* wire bond pads are also included in the layout of the biosensor. The complete layout consists of 4 beam cells with different bridge dimensions.

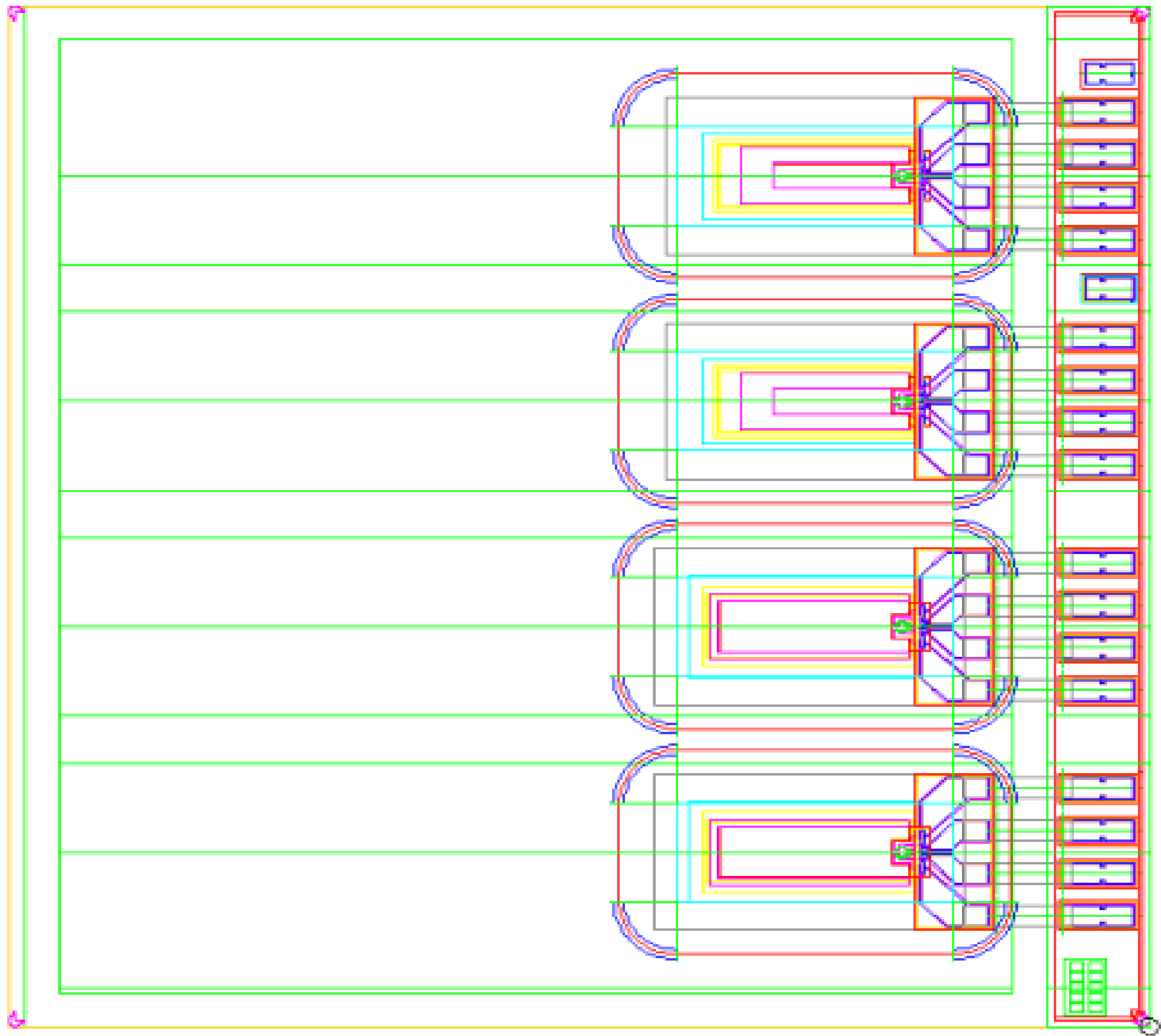

Figure 43 : Layout of the biosensor.

The layout was submitted to SensoNor for processing.

5.3 Design challenges

Many challenges were encountered in the design process. The choice of process proved to be difficult due to the difficulty of processing of the *PZT* material. Many processes were excluded because of specifications of the devices, thus finding an appropriate manufacturing process proved to be a lengthy process.

The issue whether to integrate the power management onto the same chip as the *MEMS* structure was investigated. This integration proved to be difficult using the available processes.

Additional delays in the processing of the devices made the testing process impossible in the time accorded to this work.

5.3.1 Process limitations and incompatibilities

Process limitations imposed new constraints on the dimensions of the power generator. This resulted in much shorter beams increasing the resonant frequency under which the generator would operate.

Layout rules for the metal conductors imposed a minimum width and spacing between two metal conductors of $20\mu m$. This is a serious problem for the power generator. The generated electric field is not sufficient in this case to cause a polarization in the piezoelectric material.

The incompatibility of the *MultiMems* and *SINTEF's* processes made the post-processing of the *PZT* material impossible. For this reason, a piezoresistive bridge was added to one of the beams of the power generator, interdigitated electrodes defying the absolute design rules were added to the second beam. This was done to verify the state and dimensions of the electrodes after processing. The remaining two beams were left without any electrical connection, these beams can be used to measure deflection, stress and resonant frequencies. The glass cavity above the cantilevers is sealed making any other post-processing impossible.

5.4 Conclusions

The design of the power generator was performed using modeling and simulations in order to determine the dimensions needed to operate in low frequencies. These dimensions could not be implemented in the *MultiMems* process due to fabrication constraints. A new set of dimensions were then determined according to the absolute design rules of the *MultiMems* process. A layout was constructed using the new dimensions and submitted to *SensoNor*. Layout of the biosensor was performed as well.

Due to the difficulty of the post-processing of the power generator, a piezoresistive bridge was added to one of the beams of the power generator, on the second beam, interdigitated electrodes were deposited. The last cantilevers were left without electrical contacts.

The layout of the biosensor was successfully performed according to the provided specifications.

The layout of the power generator and the biosensor was submitted to SensoNor for processing. Expected delivery is estimated in end of October according to [*31*].

6 Conclusions

6.1 Discussions

The choice of process was not determined in the beginning of this work, this choice proved to be difficult because of the processing of the piezoelectric materials. Deposition of *PZT* is however possible at *SINTEF* which was chosen for the post-processing. An additional process needed to be used for the processing of the cantilever structures. The choice of fabrication process was limited by the available *MPW* which are not very flexible. The MultiMems process by Sensonor was finally chosen because of the small membrane thickness available and the possible financing of the project by *SINTEF*.

The process imposed a set of constraints on the design. The width of the membrane of the cantilever was $3.2\mu m$. This imposed constraints on the dimensions of the beam, shorter beams can be used for thinner membranes. The thickness of the mass was also a problem, a predefined thickness of $23\mu m$ was used in the design. Because of this limitation the masses could only be expanded longitudinally which results in the increase of the stiffness of the beam and higher resonance frequencies. The use of larger masses would decrease the resonance frequency considerably. The constraint on the load applied was also too high, limiting the size of possible structures; longer beams can not withstand this pressure.

As a conclusion, the *MultiMems* process is not suitable for the design of structures resonating at low frequencies. As a solution, shorter beams were designed in order to be able to use this process. Processing is an important aspect of this work so it was decided to keep the process despite its limitations. An additional design was submitted in order to process a fully functional device.

An other important setback was the inability of *SINTEF* to post-process the power generator. Even with the constraints on the size, the device could still be used as a power generator provided the piezoelectric material was deposited. Devices with similar

dimensions as the cantilevers designed show promising results. Devices with power densities of $0.74\,mW-h/cm^2$ resonating at $13.9\,kHz$ have been constructed [2]. *SINTEF* and *Sensonor* are working on resolving incompatibility issues but much work is still to be done.

Despite these challenges, both designs were submitted for fabrication and the resulting chips are expected in October.

6.2 Future work

Further work is still possible on both designs. For the power generator design, the following steps can be studied :

- Measurement of deflection, using optical detection.
- Measurements on the piezoresistive bridge.
- The design of the power management circuit.
- Development of a custom process in order to realize the desired structures with desired dimensions.

Such a customized process could be designed through *SINTEF* or the university, which both have processing capabilities. The *MINA*-lab of the university is however not fully operational yet.

As for the biosensor, measurement on the different cantilevers is possible. Optical detection ca be used to measure deflection. Performance of the piezoresistive bridges can also be verified.

Bibliography

[1] E. M. Yeatman, "Advances in power sources for wireless sensor nodes", proceedings of the 1st International Workshop on Body Sensor Networks, 6-7 April 2004.

[2] Shad Roundy, 'pervasive computing, Improving Power Output for Vibration-Based Energy Scavengers', 2005.

[3] S. Roundy, P. Wright, J. Rabaey: "A Study Of Low Level Vibrations as a Power Source for Wireless Sensor Nodes". Computer Communications (2003)

[4] IEEE standard 176, 'IEEE Standards on Piezoelectricity', The Institute of Electrical and Electronics Engineers 1978.

[5] N. Setter. 'Piezoelectric Materials in Devices, chapter ABC of Piezoelectricity and Piezoelectric Materials', N. Setter EPFL 2002.

[6] PI Ceramics : www.piceramic.de web site, 2006.

[7] Morgan electroceramics : www.morganelectroceramics.com , 2006.

[8] Ferroperm Piezoceramics : www.ferroperm-piezo.com Web Site. 2006.

[9] Stephen R. Platt, Shane Farritor, and Hani Haider, 'On Low-Frequency Electric Power Generation With PZT Ceramics' ,April 2005 .

[10] Y.B. Jeon a, R. Soodb, J.-h. Jeong c, S.-G. Kimd, 'MEMS power generator with transverse mode thin film PZT', 2005.

[11] Wikipedia : www.wikipedia.com , web site. 2006.

[12] Fiona Lowrie, Centre for Materials Measurement & Technology, 'Time Dependent Behavior of Piezo-Electric Materials', 1999.

[13] S. TROLIER-MCKINSTRY 1 & P. MURALT, Journal of Electroceramics, 12, 7–17, 2004 Thin Film Piezoelectrics for MEMS

[14] Zhang, Q.Q., Gross, S.J., Tadigadapa, S., Jackson, T.N., Diuth, F.T., and Trolier-McKinstry, S.(2003). Lead Zirconate Titanate Films for d33 Mode Cantilever Actuators. Sensors and Actuators A: Physical, v 105 (1), p 91-7.

[15] Energy Harvesting MEMS Devices Based on d_{33} Mode Piezoelectric $Pb(Zr,Ti)O_3$ Thin Film Cantilever Yongbae Jeon, Rajendra Sood, Lodewyk

Steyn, and Sang-Gook Kim , Micro and Nano Systems Laboratory, Dept. of Mechanical Engineering Massachusetts Institute of Technology, November, 2003

[16] www.bluetooth.com/bluetooth/

[17] www.zigbee.org/en/index.asp

[18] S. Roundy and P.K. Wright, "A piezoelectric vibration based generator for wireless electronics," Smart Materials and Structures, vol. 13, 2004.

[19] Platt S R, Farritor S and Haider H 2005a On low-frequency electric power generation with PZT ceramics IEEE/ASME Trans. Mechatronics

[21] 'Analytical Modeling of beam behavior under different actuations'
E. Sarraute and I. Dufour.

[22] SCAVENGING ENERGY FROM PIEZOELECTRIC MATERIALS FOR WIRELESS SENSOR APPLICATIONS. Christoffer green, Karla M. Mossi, Robert G. Bryan, november 2005

[23] Lefeuvre E, Badel A, Benayad A, Lebrun L, Richard C and Guyomar D 2005a A comparison between several approaches of piezoelectric energy harvesting J. Physique Coll. **128** 177–86

[24] 'A simple and powerful analytical model for MEMS piezoelectric' multimorphs
W.E. Booij1, A.H. Vogl1*, D.T. Wang1, F. Tyholdt , N.P. Østbø1, H. Ræder and K. Prume SINTEF, 2aixACCT Systems GmbH,

[25] www.azom.com/details.asp?ArticleID=133

[26] www.coventor.com/

[27] www.cantion.com

[28] www.tronics-mst.com

[29]sni.nextframe.net/index.html

[30] MultiMems design handbook.

[31] www.multimems.com/Schedule/Schedule.htm

Appendix

***Hard* Materials**

PZT-4 This material is ideally suited for ultrasonic cleaning, sonar, and other high power acoustic radiation applications. These materials are designated as *PZT*-4 type materials and are capable of producing large mechanical drive amplitudes while maintaining low mechanical and dielectric losses. In addition, it can be used under both constant and repetitive conditions. Within this group of materials, a complete range of eight *PZT*-4 material types with a variety of permittivity values is available, coupling, power handling and actuation properties.

PZT-8 This material is used in high power applications, even though its piezoelectric activity level is slightly lower than *PZT*-4 types. With an extremely high mechanical quality and extremely low loss factor, *PZT*-8 materials have the ultimate power handling capability. Within this group of materials, a complete range of eight *PZT*8 material types with a variety of permittivity values, coupling, power handling and actuation properties is available.

PC3 This material is a barium titanate ceramic that is still used for a variety of sonar and specialized transducer applications.

***Soft* Materials**

PZT-5A/PC5 This material is used as the receiver or generator element in hydrophones, accelerometers, and vibration pickups. These materials have high sensitivity, permittivity, time stability and can withstand relatively high temperatures in application.

PZT-5J This material is used in fuses, hydrophones, and other applications that require a combination of high energy and high voltage output. it has high permittivity and a high piezoelectric voltage constant.

PZT-5H This material is used in sensitive receivers and applications requiring fine movement control. It has been used in a wide range of applications from hydrophones to ink jet printers. *PZT*-5H provides extremely high permittivity, coupling, and piezoelectric constant.

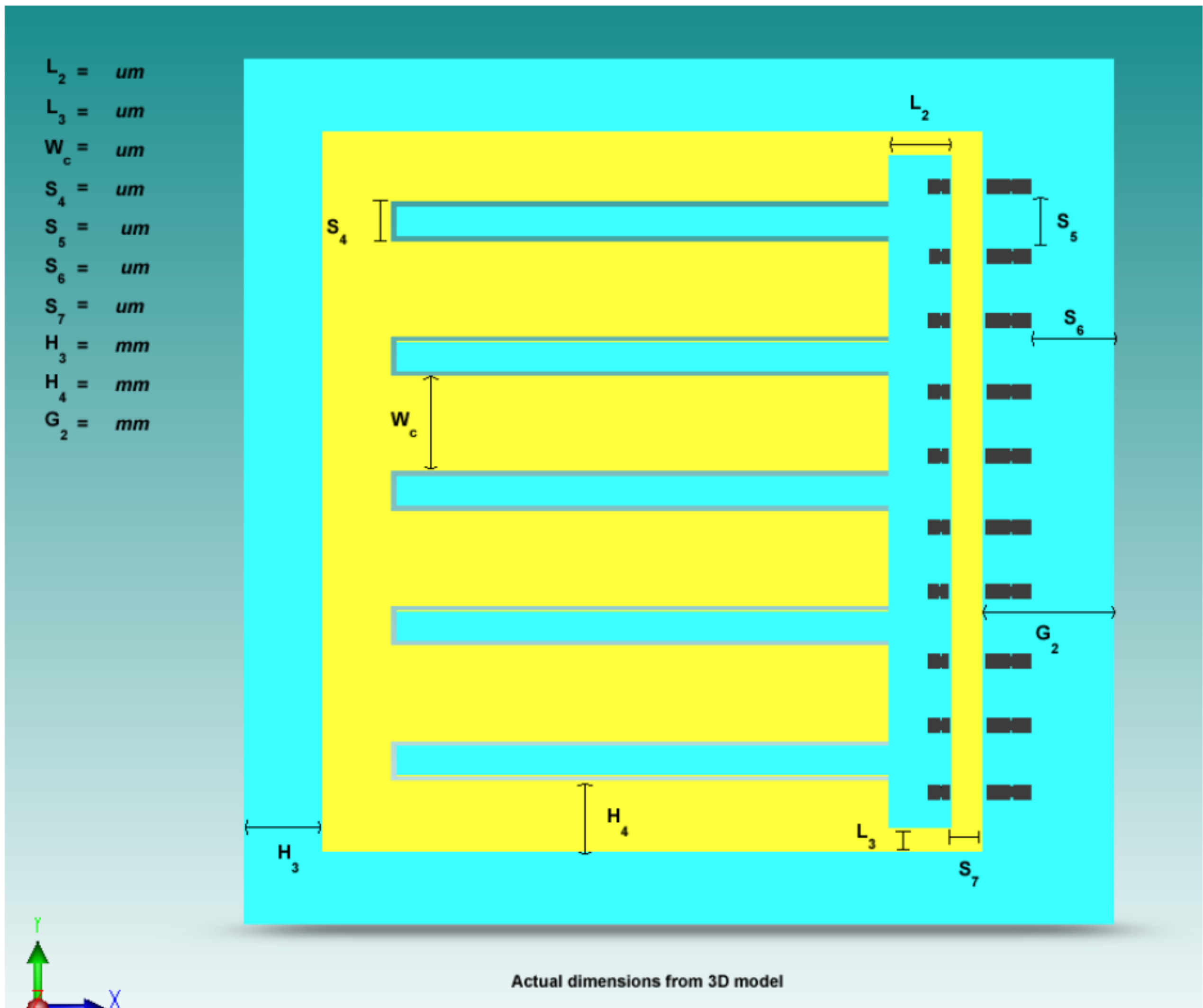

Top view of the 3-d model of the initial setup

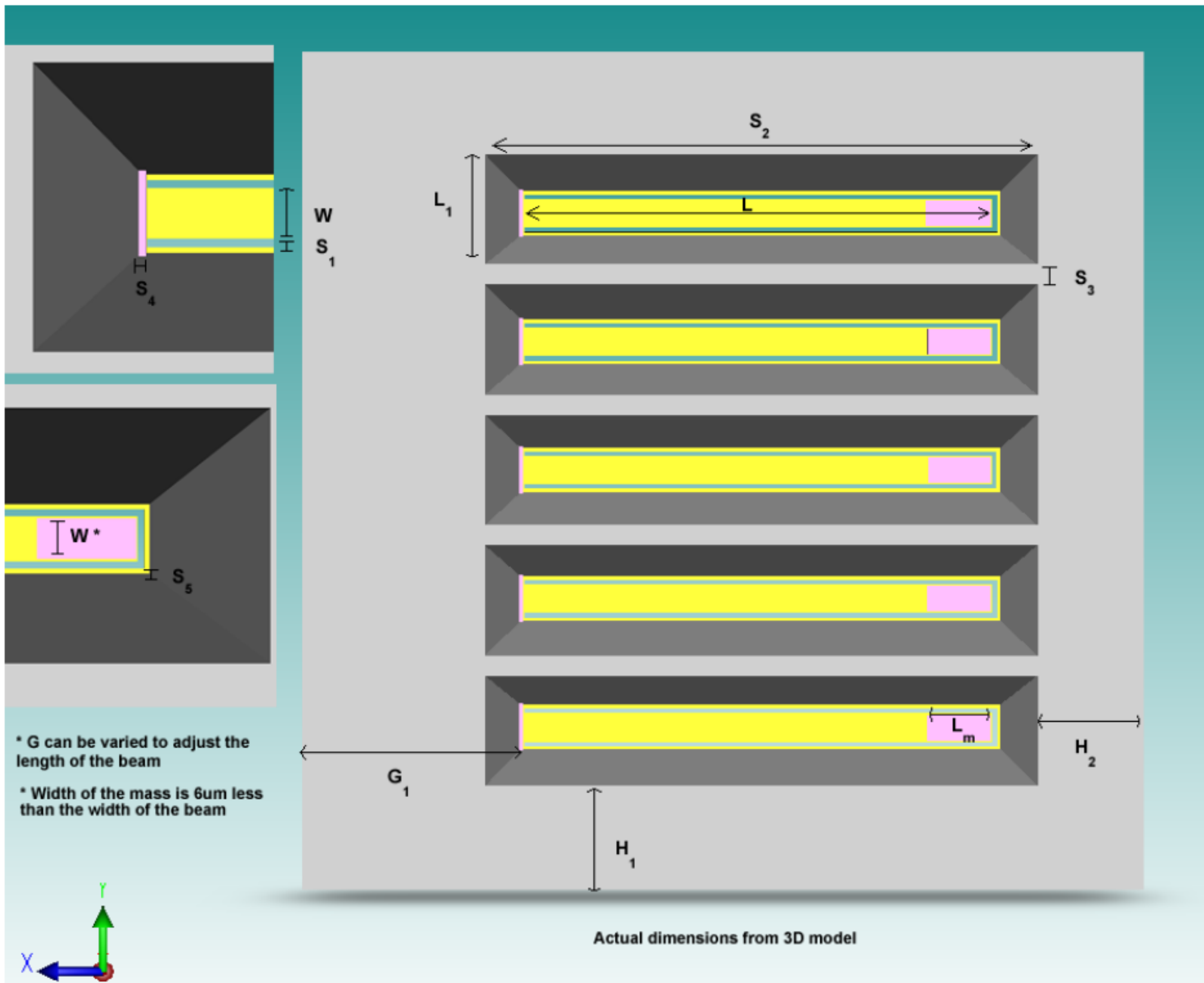

Bottom view of the 3-d model of the initial setup

Snapshots of the simulations

Length simulations

Resulting frequencies for length variations.

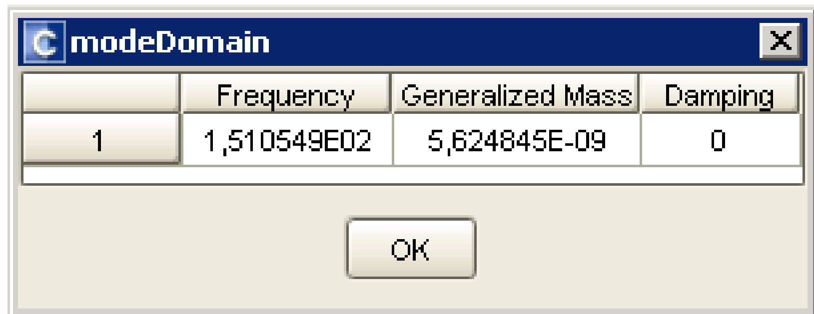

	Frequency	Generalized Mass	Damping
1	1,510549E02	5,624845E-09	0

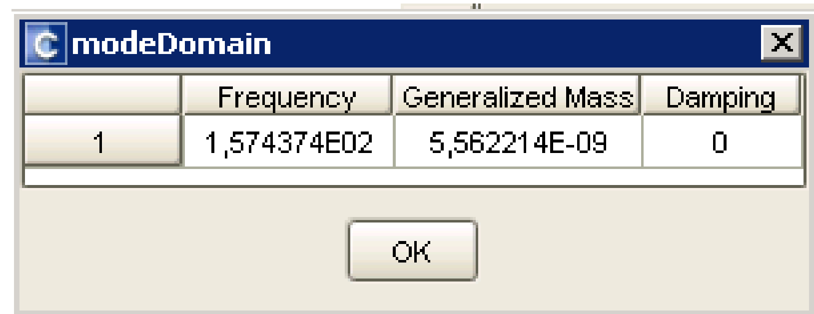

	Frequency	Generalized Mass	Damping
1	1,574374E02	5,562214E-09	0

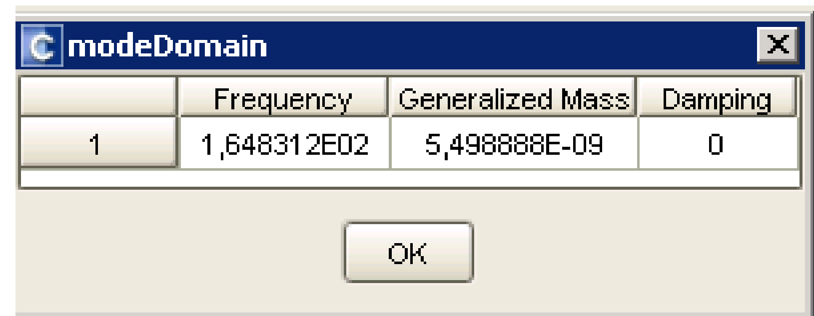

	Frequency	Generalized Mass	Damping
1	1,648312E02	5,498888E-09	0

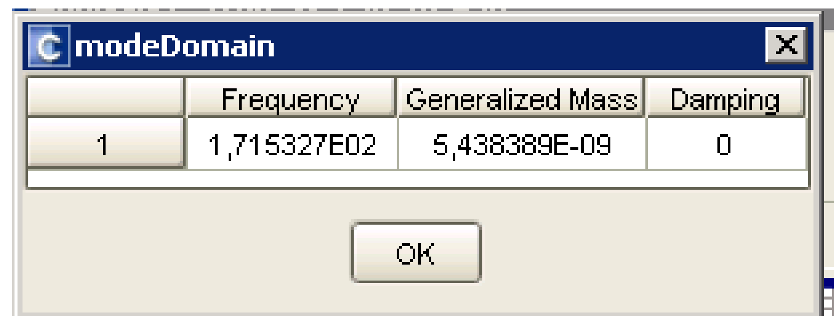

	Frequency	Generalized Mass	Damping
1	1,715327E02	5,438389E-09	0

modeDomain

	Frequency	Generalized Mass	Damping
1	1,789026E02	5,380413E-09	0

OK

modeDomain

	Frequency	Generalized Mass	Damping
1	1,882028E02	5,31374E-09	0

OK

Alternate dimensions

modeDomain

	Frequency	Generalized Mass	Damping
1	1,894287E03	3,000829E-09	0

OK

modeDomain

	Frequency	Generalized Mass	Damping
1	3,362184E03	5,908987E-10	0

OK

modeDomain

	Frequency	Generalized Mass	Damping
1	8,532202E03	4,254727E-10	0

OK

Biosensor simulations

modeDomain

	Frequency	Generalized Mass	Damping
1	8,868913E03	1,979796E-10	0

OK

modeDomain

	Frequency	Generalized Mass	Damping
1	4,304558E03	5,722411E-10	0

OK

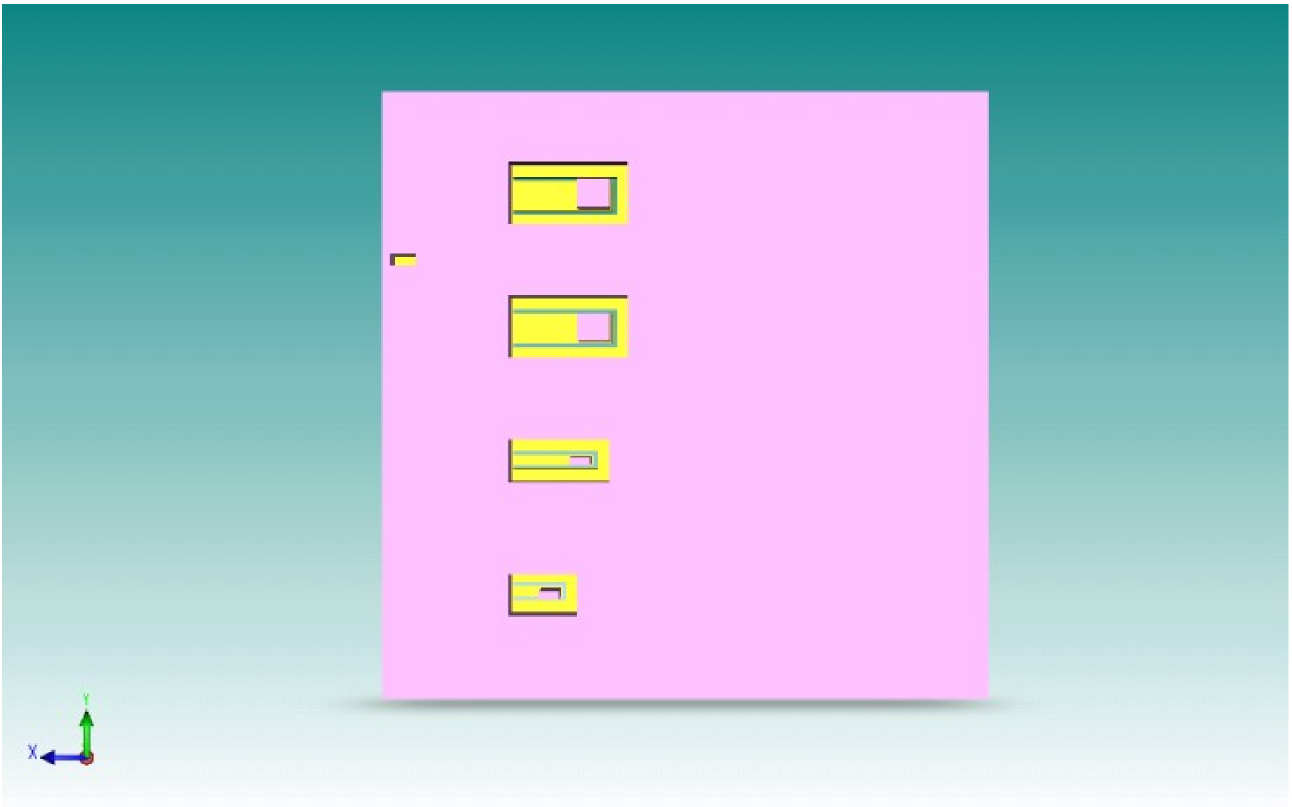

Bottom view of the 3-d model of the alternate design.

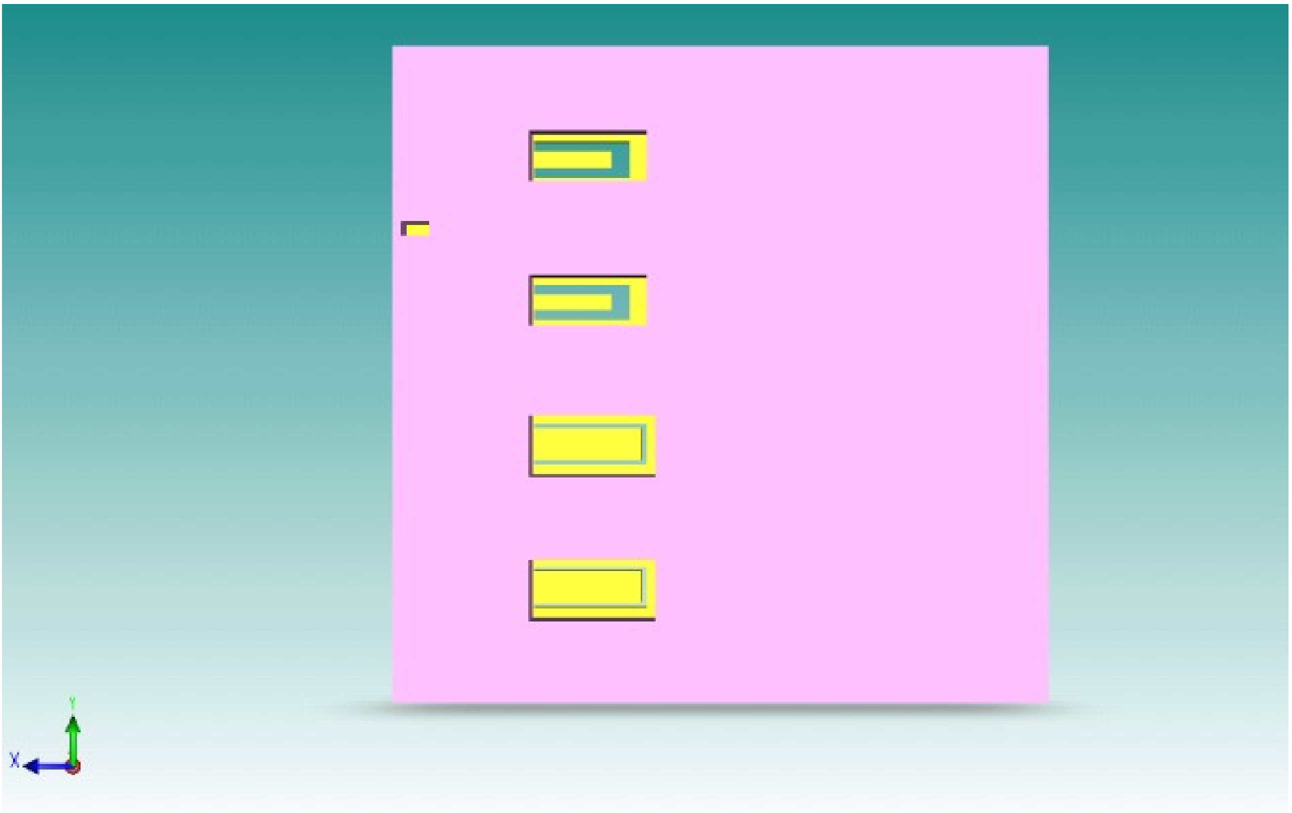

Bottom view of the 3-d model of the biosensor.

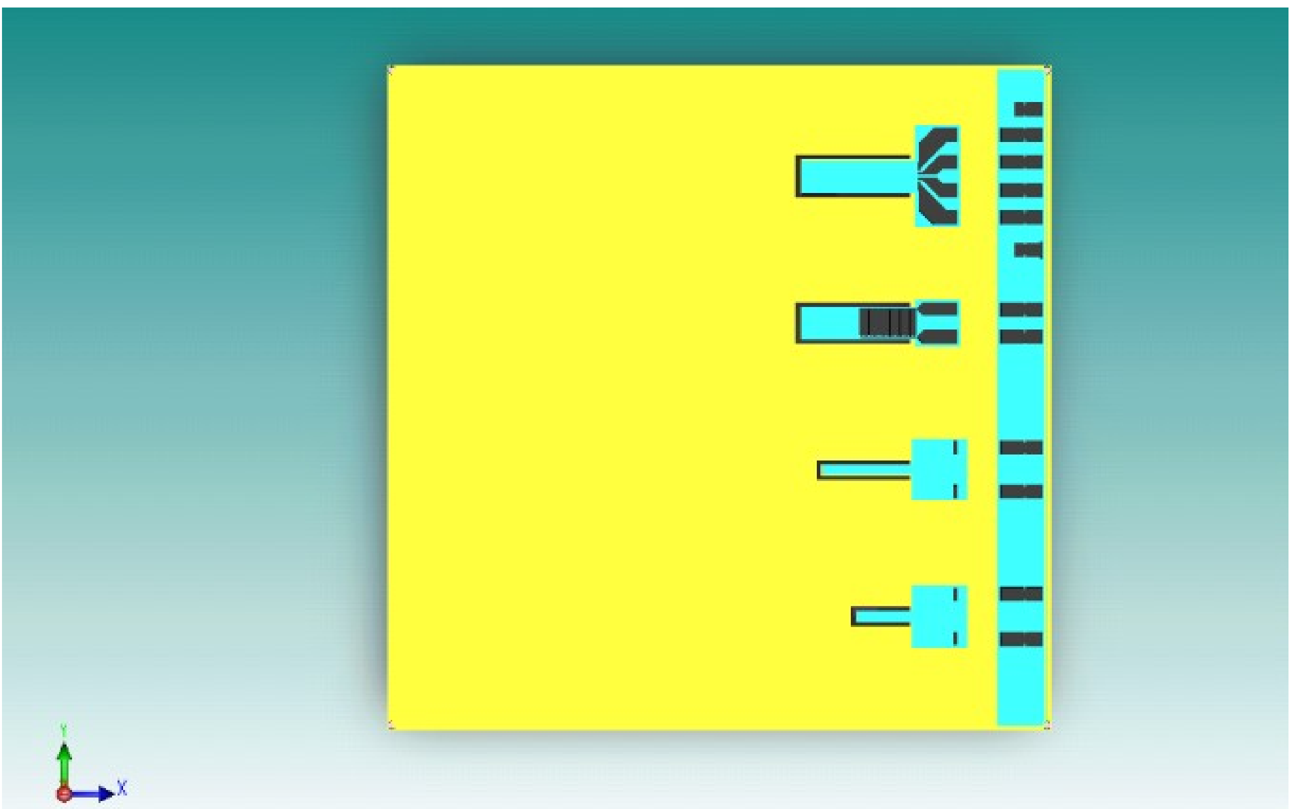

Top view of the 3-d model of the alternate design.

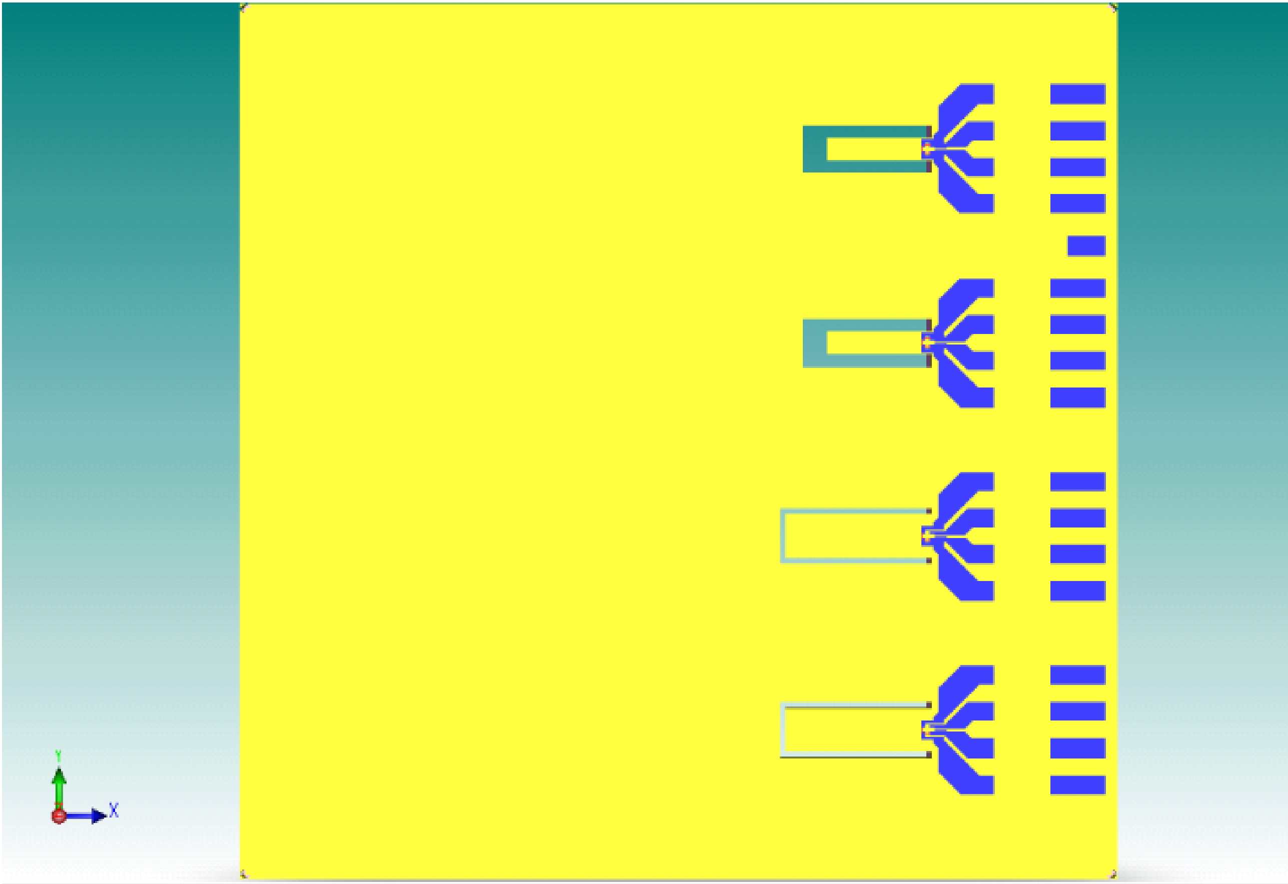

Top view of the 3-d model of the biosensor.

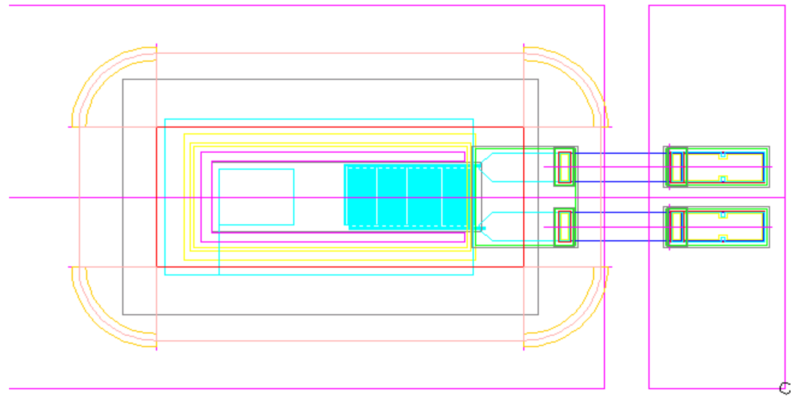

Layout of a beam cell with IDT electrodes

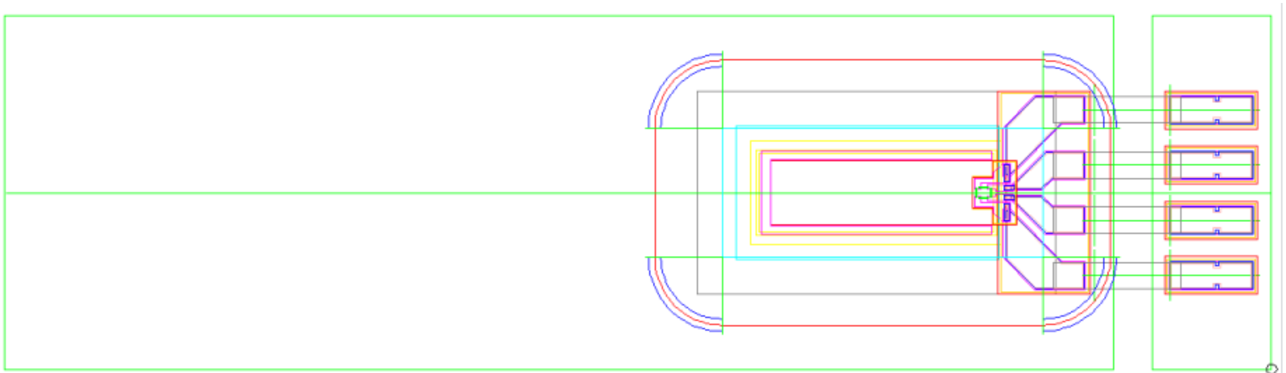

Layout of beam cell with piezoresistive bridge.

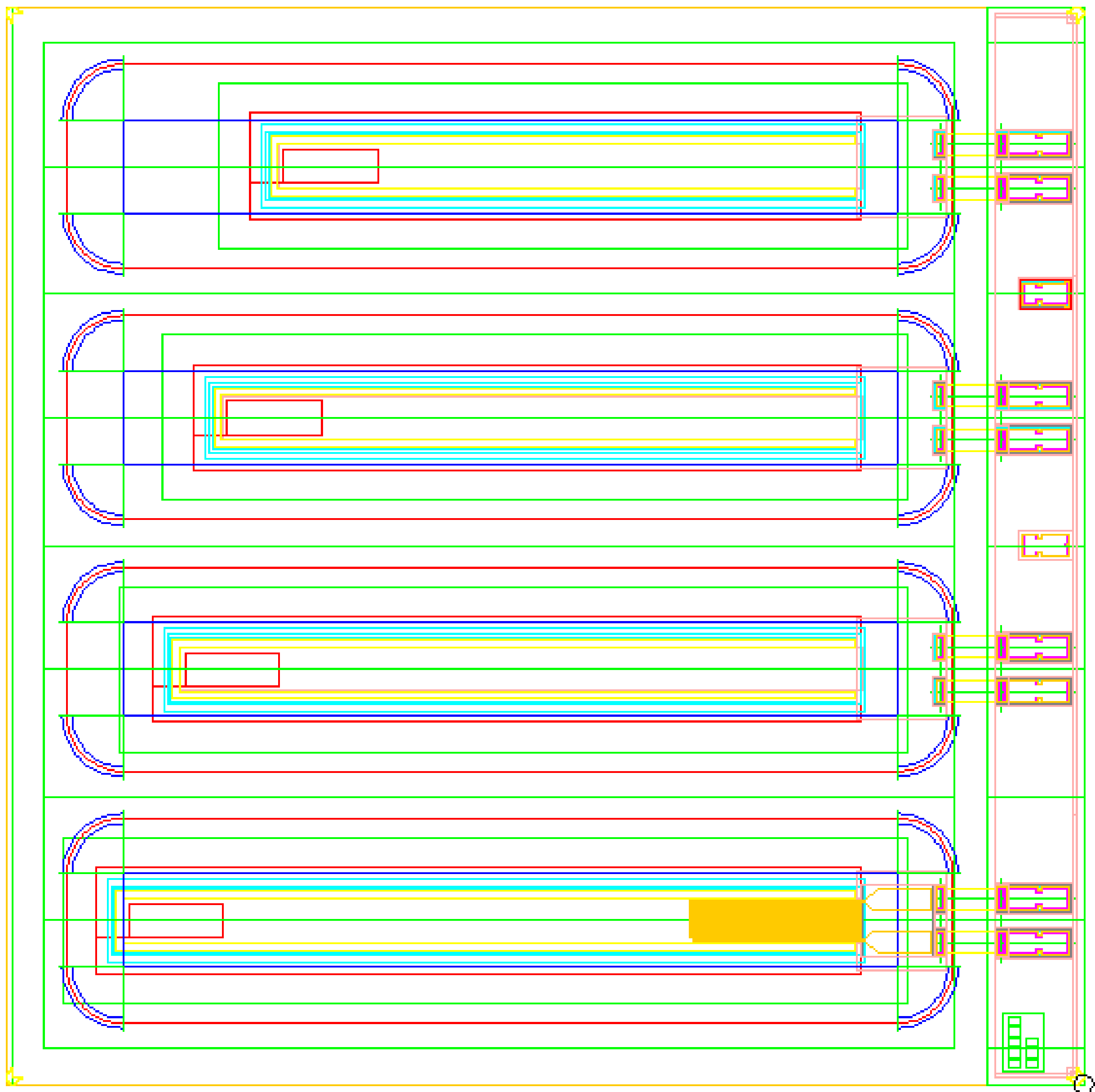

Layout of the initial design.